Research Square

Preprints are preliminary reports that have not undergone peer review.
They should not be considered conclusive, used to inform clinical practice,
or referenced by the media as validated information.

# Activity-dependent presynaptic proteomics reveals a prefrontal–amygdala release-site programme for remote contextual recall

**Tetsuya Takano**

tetsuya.takano@bioreg.kyushu-u.ac.jp

Kyushu University https://orcid.org/0000-0002-2599-3155

**Sayaka Nagamoto**

Kyushu University

**Yuki Ito**

Kyushu University https://orcid.org/0000-0002-9113-982X

**Akari Fukuda**

Kyushu University

**Junpei Matsubayashi**

Kyushu University

**Shota Morikawa**

The University of Tokyo

**Kohei Onishi**

Molecular Mechanisms of Brain Development, Center for Brain Science (CBS), RIKEN
https://orcid.org/0000-0001-5811-4607

**Mizuki Funakosi**

Kyushu University

**Scott Soderling**

Duke University Medical Center

**Haruki Takeuchi**

University of Tokyo

**Yuji Ikegaya**

The University of Tokyo https://orcid.org/0000-0003-2260-8191

**Tomomi Shimogori**

RIKEN institute

**Hidetaka Kosako**

Tokushima Univ. https://orcid.org/0000-0003-3228-6368

**Biological Sciences - Article**

**Keywords:**

**Posted Date:** November 11th, 2026

**DOI:** https://doi.org/10.21203/rs.3.rs-8597698/v2

**License:** This work is licensed under a Creative Commons Attribution 4.0 International License.
Read Full License

**Additional Declarations:** The authors declare no competing interests.

# Activity-dependent presynaptic proteomics reveals a prefrontal–amygdala release-site programme for remote contextual recall

**Sayaka Nagamoto[1,2,†], Yuki Ito[1,2,†], Akari Fukuda[1,2,†], Junpei Matsubayashi[1,2,†], Shota Morikawa[3], Kohei Onishi[4], Mizuki Funakoshi[1,2], Asumi Iwasaki[1,2], Ayako Fujisaki[1,2], Scott H Soderling[5,6], Haruki Takeuchi[3], Yuji Ikegaya[7,8,9], Tomomi Shimogori[4], Hidetaka Kosako[10] and Tetsuya Takano[1,2,11*]**

1. Kyushu University Institute for Advanced Study, 3-1-1 Maidashi, Higashi-ku, Fukuoka, 812-8582, Japan.
2. Division of Molecular Systems for Brain Function, Kyushu University Medical Institute of Bioregulation 3-1-1 Maidashi, Higashi-ku, Fukuoka, 812-8582, Japan.
3. Laboratory of Molecular Neurobiology, Department of Biophysics and Biochemistry, The University of Tokyo, Bunkyo-ku, Tokyo, 113-0032, Japan.
4. Molecular Mechanisms of Brain Development, Center for Brain Science (CBS), RIKEN, 2-1 Hirosawa, Wako, Saitama 351-0198, Japan.
5. Department of Cell Biology, Duke University Medical School, Durham, NC 27710, USA
6. Department of Neurobiology, Duke University Medical School, Durham, NC, 27710, USA
7. Graduate School of Pharmaceutical Sciences, The University of Tokyo, Tokyo 113-0033, Japan.
8. Institute for AI and Beyond, The University of Tokyo, Tokyo 113-0033, Japan.
9. Center for Information and Neural Networks, National Institute of Information and Communications Technology, Suita City, Osaka 565-0871, Japan.
10. Division of Cell Signaling, Institute of Advanced Medical Sciences, Tokushima University, Tokushima 770-8503, Japan.
11. PRESTO, Japan Science and Technology Agency, 4-1-8 Honcho, Kawaguchi, Saitama 332-0012, Japan.

[†]These authors contributed equally

* Corresponding author: Tetsuya Takano, Division of Molecular Systems for Brain Function, Kyushu University Institute for Advanced Study, 3-1-1 Maidashi, Higashi-ku, Fukuoka, 812-8582, Japan.

E-mail: tetsuya.takano@bioreg.kyushu-u.ac.jp

**Abstract**

Remote memory retrieval engages distributed neuronal ensembles, yet how these ensembles organise long-range circuit output at the presynaptic molecular level remains poorly understood. Here, we develop Activity-dependent Projection-eXclusive BioID (ActProX-ID), an *in vivo* proximity-labelling strategy that combines TRAP2-dependent capture of behaviourally activated neurons with presynaptic membrane-targeted TurboID to profile projection-level, presynaptically enriched proteomic states. Application of ActProX-ID to the medial prefrontal cortex (mPFC)–basolateral amygdala (BLA) pathway during recent and remote fear-memory recall identified overlapping but phase-biased presynaptic programmes. Recent recall was associated with cytoskeletal and synaptic-organisation proteins, whereas remote recall preferentially engaged synaptic vesicle trafficking, transmembrane transport and release-site organisation. Subsequent analyses under remote contextual recall validated TSPAN7 as a remote recall-associated presynaptic component at mPFC–BLA terminals. TSPAN7 loss or expression of the disease-linked P172H variant impaired recall-associated synaptic remodelling, CPLX2 recruitment, SNAP25-positive release-site organisation and presynaptic release efficacy, and disrupted remote contextual fear memory while sparing recent contextual and tone-cued fear memory. These findings link behaviourally recruited prefrontal projection neurons to presynaptic molecular remodelling and reveal a TSPAN7–CPLX2-dependent release-site mechanism that controls remote contextual recall.

## Main

Long-term memory is thought to depend on the reactivation and progressive reorganisation of sparsely distributed neuronal ensembles, often referred to as engram cells, whose connectivity and synaptic efficacy are reshaped as memories mature[1–3]. Activity-dependent tagging studies have shown that prelimbic and broader medial prefrontal cortex (mPFC) ensembles become increasingly engaged during remote memory retrieval[4–6]. These cortical ensembles are thought to influence memory expression through long-range projections to downstream structures, including the basolateral amygdala (BLA), a major node for emotional memory and contextual fear recall[7–10]. Although the cellular dynamics of recall-associated ensembles have been extensively examined, it remains unclear how these ensembles organise their output at the presynaptic terminals of defined long-range projections. Thus, the presynaptic molecular architectures that support communication through recall-engaged prefrontal projections remain poorly understood.

Activity-dependent genetic tagging approaches, including targeted recombination in active populations (TRAP), provide genetic access to neuronal populations recruited by defined experiences and have revealed dynamic reorganisation of memory-related ensembles during learning and recall[4,5,11]. Bulk, single-cell and spatial transcriptomic analyses of TRAP- or engram-tagged neurons have further identified persistent transcriptional programmes associated with synaptic plasticity, vesicle trafficking, local translation and structural remodelling after learning[12–15]. These studies have been essential for defining molecular states of memory-related neuronal ensembles. However, transcriptomic approaches are not designed to resolve the local protein composition of presynaptic boutons within a defined projection, nor do they by themselves reveal how release-related machinery is organised at synapses engaged during recall. This distinction is important because projection output is implemented in part through local mechanisms at presynaptic terminals, where vesicle cycling, release-site organisation and short-term release properties shape synaptic efficacy during retrieval[16,17]. Moreover, in long-range axons, local translation, trafficking and degradation are compartmentalised, meaning that mRNA abundance may not fully capture local presynaptic protein composition[18–21]. Therefore, complementary strategies that connect behaviourally recruited projection neurons to their presynaptic proteomic states *in vivo* are needed to understand how molecular remodelling of long-range synapses contributes to remote-memory expression.

Proximity-dependent biotinylation approaches based on BioID and related enzymes have enabled spatially restricted proteomic analyses of genetically defined cellular compartments *in*

*vivo*[22–27]. By genetically fusing promiscuous biotin ligases to proteins that localize to selected subcellular domains, these methods enable covalent labelling and mass spectrometric identification of proteins within native molecular neighbourhoods in intact tissue [22–25]. We and others have used proximity labelling to define synaptic protein complexes, and glial–neuronal contact sites *in vivo*, establishing spatial proteomics as a powerful approach for mapping molecular organisation in neural circuits[28–32]. However, it has remained difficult to link activity-defined neuronal ensembles to projection-level presynaptic proteomic states during behaviourally defined recall phases. Building on this spatial proteomics framework, we recently developed Projection-eXclusive BioID (ProX-ID), which targets a highly active biotin ligase to presynaptic membrane-associated compartments of anatomically defined projection neurons and enables projection-targeted, presynaptically enriched proteomic profiling *in vivo*[33]. Here, we extend this strategy by developing Activity-dependent Projection-eXclusive BioID (ActProX-ID), which combines ProX-ID-based presynaptic labelling with TRAP2-dependent ensemble capture. Because TRAP2-dependent recombination, reporter expression and TurboID-mediated biotinylation occur over time, ActProX-ID provides a presynaptically enriched proteomic readout from projection neurons genetically captured during recall-associated activity, rather than an instantaneous snapshot of the proteome at the moment of recall.

We applied ActProX-ID to the mPFC–BLA pathway to profile presynaptic proteomic states associated with recent and remote fear-memory recall. Although many recall-enriched proteins were shared between the two phases, phase-preferential subsets highlighted functional biases in the recall-associated presynaptic proteome. Recent recall was associated with cytoskeletal and synaptic-organisation programmes, whereas remote recall was preferentially associated with synaptic vesicle trafficking, transmembrane transport and release-site organisation. Candidates from this screen were then tested under remote contextual recall, a memory condition closely linked to prelimbic cortical ensembles and mPFC–BLA circuit interactions. This analysis identified TSPAN7 as a presynaptic component preferentially associated with remote recall in this pathway. During remote contextual recall, TSPAN7 accumulated at mPFC–BLA terminals and was required for CPLX2 recruitment, SNAP25-positive release-site organisation and recall-associated synaptic remodelling. Disruption of TSPAN7 or expression of the disease-linked P172H variant impaired remote contextual fear memory while sparing recent contextual and tone-cued fear memory. Together, these findings link behaviourally recruited prefrontal projection neurons to presynaptic molecular

remodelling and reveal a TSPAN7–CPLX2-dependent release-site mechanism supporting remote contextual memory.

## Results

*ActProX-ID enables activity- and projection-resolved presynaptic proteomics*

To define presynaptic proteomes associated with behaviourally activated projection neurons, we developed Activity-dependent Projection-eXclusive BioID (ActProX-ID), an activity-gated extension of ProX-ID (Fig. 1a). ProX-ID enables *in vivo* proximity labelling of proteins in anatomically defined projection pathways by targeting a biotin ligase to presynaptic membrane-associated compartments through the palmitoylation sequence of GAP43[33]. ActProX-ID builds on this strategy by combining presynaptic membrane targeting with TRAP2-dependent genetic access to neurons activated during a defined behavioural epoch. In this system, 4-hydroxytamoxifen (4-OHT) enables CreERT2-mediated recombination in cFos-expressing neurons, thereby inducing Cre-dependent expression of presynaptically targeted TurboID, a highly active biotin ligase. Subsequent systemic biotin administration allows biotinylation of proteins in presynaptically enriched compartments of BLA projections from behaviourally recruited mPFC neurons. Thus, ActProX-ID was designed to profile presynaptic proteomes in mPFC–BLA projections from neurons genetically captured during fear-memory recall (Fig. 1a). We applied ActProX-ID to the mPFC–BLA pathway to profile presynaptic proteomes associated with recent and remote fear-memory recall (Fig. 1b). In adult TRAP2 (cFos–CreERT2) mice (6 weeks old), a Cre-dependent neuron-specific ActProX-ID construct (AAV-PHP.eB-CaMKII-DIO-ActProX-ID) was injected into the prelimbic (PrL) region of the mPFC (Fig. 1a). Mice then underwent differential auditory fear conditioning on day 0, in which a conditioned tone (CS+) was paired with foot shocks, whereas a second auditory cue (CS–) was presented without reinforcement in the same context. On day 1 (recent fear memory recall, FR-S) or day 14 (remote fear memory recall, FR-L), mice received 4-OHT 1 h before tone-cued recall in the same context. Home-cage (HC) and no-fear (NF; CS+ tone exposure without prior fear conditioning) cohorts served as controls (Fig. 1b). Freezing during CS+ presentation was similar in FR-S and FR-L mice and negligible in NF controls, indicating that the molecular differences observed thereafter were unlikely to reflect differences in behavioural expression during retrieval (Extended Data Fig. 1a). The following day, mice received biotin, and BLA tissues were microdissected and collected 6 h later. Biochemical enrichment showed a marked increase in biotinylated proteins in FR-S and FR-L mice relative to NF controls, with ActProX-ID expressed in the mPFC (Extended Data Fig. 1b,c). In NF mice, biotinylated protein

enrichment remained near background levels (Extended Data Fig. 1b,c). Immunohistochemical analysis of the mPFC injection site confirmed ActProX-ID reporter expression in the PrL of 4-OHT-treated mice, with prominent local streptavidin signal in FR-S and FR-L samples and only weak signal in NF controls (Extended Data Fig. 1d). In the BLA, strong streptavidin labelling was observed in FR-S and FR-L mice, but not in HC or NF mice (Extended Data Fig. 1e,f), indicating recall-associated biotinylation in the BLA projection fields of ActProX-ID-expressing mPFC neurons. We next examined whether this labelling was concentrated at presynaptic compartments. Super-resolution STED microscopy visualised bouton-like ActProX-ID puncta at mPFC–BLA presynaptic terminals (Fig. 1c). To further assess the subcellular distribution of ActProX-ID labelling in BLA projections from recall-captured mPFC neurons, we performed biochemical fractionation of microdissected BLA tissue and isolated synaptosome-enriched fractions from FR-S and FR-L mice. In both conditions, biotinylated proteins were enriched in the synaptosome fraction together with the excitatory synaptic markers VGLUT1 and Homer1, whereas signals in the cytosolic fraction (S2) remained comparatively weak (Extended Data Fig. 1g,h). ActProX-ID itself was also detected predominantly in membrane-associated fractions, including the synaptosome fraction (Extended Data Fig. 1g ). These fractionation profiles indicate that ActProX-ID labelling was concentrated in synaptosome-enriched membrane compartments rather than diffusely distributed across soluble cytosolic fractions. Consistent with these biochemical results, immunohistochemical analysis showed that biotinylated proteins were highly colocalised with VGLUT1-positive presynaptic terminals in both FR-S and FR-L mice, with more than 77% of biotinylated puncta overlapping VGLUT1-positive structures (Extended Data Fig. 1i-k). This degree of colocalisation was comparable to that observed for ActProX-ID-positive puncta themselves (Extended Data Fig. 1j-k). Together, these results support the preferential enrichment of ActProX-ID labelling at mPFC–BLA presynaptic terminals from recall-captured mPFC neurons.

Having validated projection-targeted labelling with preferential enrichment in presynaptic compartments, we next used ActProX-ID for proteome-wide discovery across recall phases (Fig. 1b). To profile recall-associated presynaptic proteomes in the mPFC–BLA pathway, we isolated biotinylated proteins from microdissected BLA tissue of HC, NF, FR-S and FR-L mice by streptavidin affinity purification, followed by on-bead digestion and quantitative DIA-based LC–MS/MS analysis (Fig. 1b). A total of 3,767 unique proteins were detected across conditions. NF mice showed biotinylation levels near HC background levels, and few proteins met our significance threshold ($\log_2FC > 2.0$, $P < 0.05$ versus HC), indicating

minimal activity-dependent labelling without fear conditioning (Extended Data Fig. 2a–c; Extended Data Table 1). We then defined recall-enriched biotinylated proteins as proteins increased in FR-S or FR-L relative to both HC and NF controls ($log_2FC > 2.0$, $P < 0.05$; Extended Data Table 1). Using this criterion, we identified 458 and 392 recall-enriched proteins in the FR-S and FR-L groups, respectively (Fig. 1d,e). These datasets shared 347 proteins (Fig. 1e), of which only three significantly differed between FR-S and FR-L (Extended Data Fig. 2d), indicating that phase-related differences were mainly driven by proteins preferentially meeting the enrichment criterion in one recall phase rather than by broad abundance shifts among shared proteins. Both FR-S and FR-L datasets contained core presynaptic components, including synaptotagmins (Syts), synapsins (Syns), syntaxins (Stxs), SNAPs and VAMPs (Fig. 1f). Recall-enriched proteins also included molecules annotated by Gene Ontology (GO) as memory-related and genes previously identified by cFos-TRAP-based ensemble labelling during remote memory recall[13], providing convergent support that ActProX-ID recovers memory-associated presynaptic proteins *in vivo* (Fig. 1f). These results indicate that ActProX-ID enables profiling of presynaptic proteomes in recall-captured mPFC–BLA projection neurons *in vivo* and enables quantitative comparison of presynaptic molecular states across recent and remote memory recall. The ActProX-ID screen was designed to maximise recovery of recall-associated presynaptic candidates under a robust retrieval condition. Subsequent validation experiments focused on remote contextual recall, a condition more strongly linked to prelimbic cortical ensembles and mPFC–BLA circuit interactions, to test whether these candidates were functionally relevant to pathway-dependent memory recall (Supplementary Table 1).

*Network organisation of recall-associated presynaptic proteomes in the mPFC−BLA pathway*

To organise recall-associated proteins into coherent functional and structural modules within the presynaptic architecture of the mPFC−BLA pathway, we first established a network-based framework integrating functional annotations with projection-resolved context[33]. We then asked how recall-associated proteins relate to the steady-state presynaptic repertoire of the mPFC−BLA projection and whether distinct functions differentiate recent and remote recall. To place recall-associated proteins within the presynaptic architecture of the mPFC−BLA pathway, we compared ActProX-ID datasets with a steady-state projection-resolved presynaptic proteome using ProX-ID (Extended Data Fig. 2e). We identified 809 proteins enriched in steady-state ProX-ID preparations from mPFC–BLA projections ($log_2FC > 2.0$, $P$

$< 0.05$), providing a projection-resolved reference for interpreting recall-associated presynaptic proteins (Extended Data Fig. 2f,g; Extended Data Table 2). Of these ProX-ID-enriched proteins, 56, 15 and 236 overlapped with the FR-S-associated, FR-L-associated and shared FR-S/FR-L recall-responsive sets, respectively, indicating that recall engages a subset of the projection-resolved presynaptic repertoire (Extended Data Table 2).

We organised the principles within recall-associated presynaptic proteomes by constructing a protein–term network that integrated recall-associated categories (FR-S-associated, FR-L-associated or shared FR-S/FR-L), functional annotation (KEGG BRITE) and projection-resolved steady-state context (Fig. 2a; Extended Data Table 3). This framework shows that fear recall engages a presynaptic program centred on plasma membrane signalling and trafficking, with transporter-linked proteins and vesicle-handling components represented alongside canonical release machinery and neuroactive signalling molecules (Fig. 2a; Extended Data Fig. 2h–o). GO cellular component enrichment analysis showed higher odds ratios for plasma membrane localisation in the FR-S and FR-L datasets than in the steady-state ProX-ID dataset (Fig. 2b–d). STRING-derived cellular compartment scores indicated increased plasma membrane proteins in FR-S and FR-L samples (Fig. 2e), supporting the engagement of membrane-proximal signalling during recall. SynGO analysis[34] revealed greater over-representation of presynaptic than postsynaptic annotations among the identified proteins (Supplementary Fig. 1). Although a subset of proteins carried postsynaptic annotations, approximately half were also co-annotated as presynaptic, consistent with established roles on both sides of the synapse[35–37]. The remaining proteins with postsynaptic annotations may in part reflect the current bias in synaptic protein annotation towards postsynaptic compartments. We therefore further assessed presynaptic coverage using SynaptomeDB[38], which provided broader annotation coverage for the synaptic proteins identified in this study. Comparison with the SynaptomeDB database indicated that more than half of the proteins carried presynaptic annotations (Fig. 2f; Extended Data Table 2; Supplementary Fig. 2; Supplementary Table 2). Moreover, 14–20% of the proteins were poorly characterised at the functional level (see Methods), suggesting that the recall-associated presynaptic proteome contains previously uncharacterised components. In addition, 37% were associated with neurological or psychiatric disorders (Fig. 2f; Extended Data Table 2; Supplementary Fig. 2; Supplementary Table 2).

GO biological process and molecular function analyses revealed a recurrent over-representation of transporter-related functions, including inorganic molecular entity transmembrane transporter activity and transport terms across recall conditions (Fig. 2g). The two recall phases showed biased engagement in the functional programs. FR-S-associated

proteins were enriched for cytoskeletal and synaptic-organisation terms, whereas FR-L-associated proteins showed greater representation of vesicle-transport terms (Fig. 2g). Cross-species mapping supports translational relevance. Of the 503 proteins enriched in either FR-S or FR-L, 497 (98.8%) mapped to identifiable marmoset orthologues with expression in the mPFC, and many highly expressed orthologues corresponded to genes associated with human neurological or psychiatric disorders (Fig. 2h; Supplementary Table 3). These analyses indicate that recall-engaged presynaptic proteins form a functionally organised subset of the projection-resolved presynaptic repertoire, with prominent representation of membrane signalling, transport and vesicle-handling modules. They further reveal phase-biased representation of cytoskeletal and synaptic-organisation programmes during recent recall and synaptic vesicle-transport programmes during remote recall.

*TSPAN7 accumulates at recall-engaged mPFC–BLA synapses*

We searched the recall-responsive mPFC–BLA proteome for candidate regulators that could link remote memory recall to presynaptic molecular remodelling (Fig. 1–2). Among proteins enriched in the recall-associated ActProX-ID dataset, we prioritised candidates that were preferentially represented in the remote-recall dataset, had plausible roles in synaptic organisation, were genetically linked to neurodevelopmental or psychiatric disorders, and remained poorly characterised in long-range presynaptic circuits (see Methods). This analysis led us to focus on tetraspanin-7 (TSPAN7) as a candidate regulator of recall-associated presynaptic remodelling. TSPAN7 is a four-pass transmembrane protein implicated in excitatory synapse development and AMPA receptor trafficking, and pathogenic variants in TSPAN7 cause X-linked intellectual disability and have also been associated with autism spectrum disorder (Fig. 3a)[39–41]. TSPAN7 expression is increased after kainate-induced seizures[42], suggesting that its abundance or localisation may be regulated by neuronal activity. The initial ActProX-ID screen was designed to capture recall-associated presynaptic proteins under a robust retrieval condition, in which recall occurred in the conditioning context with cue presentation (context + cue recall; Fig. 1b). Streptavidin pull-downs from microdissected BLA tissue revealed recall-associated biotinylation of endogenous TSPAN7 in FR-S and FR-L mice, but not in NF controls (Extended Data Fig. 3a), indicating that TSPAN7 was recruited to ActProX-ID-labelled mPFC–BLA terminals during recall. Subcellular fractionation further showed that TSPAN7 was enriched in membrane fractions and accumulated in synaptosome-enriched fractions together with VGLUT1 and Homer1 (Extended Data Fig. 3b,c), consistent with its membrane-associated and synaptic localisation[39–41].

Because remote contextual fear recall has been linked to prelimbic cortical ensembles and mPFC–BLA circuit interactions[4,6,43], we next asked whether TSPAN7 accumulation was observed under context-only remote recall, as summarized together with the other recall conditions in Supplementary Table 1. To visualise endogenous TSPAN7 at mPFC–BLA presynaptic terminals *in vivo*, we used homology-independent universal genome engineering (HiUGE) to insert a V5 epitope into the *Tspan7* locus (Fig. 3b)[44,45]. After validating the *Tspan7*–HiUGE configuration in HEK293T cells (Extended Data Fig. 3d), we delivered an AAV encoding the *Tspan7*-targeting sgRNA and V5 donor into the mPFC of SpCas9 knock-in mice and analysed remote contextual recall (Fig. 3c). Under this condition, TSPAN7–V5 puncta were detected at mPFC presynaptic terminals within the BLA and were associated with ActProX-ID-labelled boutons (Fig. 3c,d). Quantitative analysis showed that presynaptic TSPAN7–V5 accumulation increased during remote contextual recall, and biochemical analysis likewise showed elevated endogenous TSPAN7 levels in BLA synaptosome fractions under the same condition (Fig. 3e,f). Complementing this analysis, immunohistochemical staining showed that TSPAN7-positive puncta were localised at synaptic sites during remote contextual recall, showing close association with the excitatory synaptic markers VGLUT1 and Homer1 (Extended Data Fig. 3e). We further asked whether TSPAN7 synaptic accumulation was also observed under the context + cue recall condition used for the initial ActProX-ID screen. In this paradigm, TSPAN7 showed similar recall-associated changes, including increased presynaptic TSPAN7–V5 accumulation, enrichment in synaptosome fractions (Extended Data Fig. 3f-j). Finally, to determine whether TSPAN7 preferentially associates with behaviourally reactivated synapses under the context + cue recall condition, we applied doxycycline-gated dual-eGRASP to the mPFC–BLA pathway. In this system, cyan eGRASP labels anatomically defined mPFC–BLA synaptic contacts, whereas yellow eGRASP marks synapses reactivated during remote recall (Extended Data Fig. 3k)[3,46]. TSPAN7-V5 was detected in approximately 44% of cyan-labelled contacts, whereas approximately 55% of yellow-labelled reactivated synapses were TSPAN7-V5-positive (Extended Data Fig. 3l,m), indicating preferential enrichment at behaviourally re-engaged synaptic sites. Together, these results identify TSPAN7 as an activity-regulated presynaptic component of the mPFC–BLA pathway. They further show that TSPAN7 accumulates at mPFC–BLA synapses during remote contextual recall and preferentially associates with behaviourally reactivated synaptic contacts under the context + cue recall condition.

*TSPAN7 is required for contextual recall-associated synaptic remodelling*

Having established that TSPAN7 accumulates at recall-engaged mPFC–BLA synapses, we next asked whether TSPAN7 is functionally required for recall-associated synaptic remodelling in this pathway. To manipulate TSPAN7 in mPFC projection neurons, we delivered an AAV expressing three sgRNAs targeting *Tspan7* (AAV-PHP.eB-U6-3×sgRNA-TSPAN7) into the mPFC of SpCas9 knock-in mice, thereby generating TSPAN7-deficient mPFC neurons (TSPAN7-cKO; Fig. 3g). Efficient gene disruption was verified by immunoblotting and immunohistochemistry (Extended Data Fig. 4a–c). We first examined whether TSPAN7 loss affects excitatory synapse formation in cultured neurons. TSPAN7 knockout significantly reduced excitatory synapse density, quantified as Homer1/VGLUT1-colocalised puncta along dendrites (Extended Data Fig. 4d,e). Because human genetics has identified a disease-linked P172H variant of TSPAN7 associated with neurodevelopmental disorders (Fig. 3a)[47,48], we next tested whether this mutation impairs the synaptogenic function of TSPAN7. Expression of TSPAN7 P172H in TSPAN7-depleted cultured neurons failed to rescue the reduction in Homer1/VGLUT1-positive synapses, resulting in synapse density comparable to that observed after TSPAN7 depletion (Extended Data Fig. 4d,e). We then tested whether TSPAN7 is required for recall-associated synaptic remodelling in the mPFC–BLA pathway *in vivo* under remote contextual recall conditions (Fig. 3g). To exclude the possibility that the effect of the disease-linked mutant simply reflected altered abundance or mistargeting, we expressed TSPAN7 P172H in TSPAN7-cKO mPFC projection neurons. The exogenous mutant protein was present at levels comparable to endogenous TSPAN7 in control samples and remained associated with VGLUT1-positive presynaptic structures, indicating preserved presynaptic localisation despite impaired function (Extended Data Fig. 4f–i). We next assessed excitatory synapse density in BLA regions under NF and remote contextual recall conditions, quantified as Homer1/VGLUT1-colocalised puncta (Fig. 3g). In the NF condition, excitatory synapse density, measured as Homer1/VGLUT1-colocalised puncta, was comparable across control, TSPAN7-cKO and TSPAN7 P172H mice (Fig. 3h,i). By contrast, under the FR-L condition, Homer1/VGLUT1-positive synapse density was significantly reduced in both TSPAN7-cKO and TSPAN7 P172H mice compared with controls, whereas the two TSPAN7-perturbed groups did not differ significantly from each other (Fig. 3h,j). Thus, both TSPAN7-cKO and the disease-linked P172H variant impaired remote contextual recall-associated excitatory synaptic organisation in the BLA. Presynaptic bouton volume, measured by VGLUT1 staining, was comparable across genotypes and conditions (Fig. 3k,l), indicating that TSPAN7 primarily regulates recall-associated synapse density rather than bouton size. To assess whether this defect reflected a pathway-level presynaptic impairment rather than a broad loss of excitatory

synapses in mPFC neurons, we quantified Homer1/VGLUT1-positive synapse density within the mPFC. This was unchanged across genotypes under both NF and FR-L conditions (Extended Data Fig. 5a–c), supporting the interpretation that TSPAN7 disruption preferentially impairs synaptic organisation at mPFC–BLA terminals during remote contextual recall. We further examined whether the same TSPAN7 requirement was observed under the context + cue recall condition used for the initial ActProX-ID screen (Extended Data Fig. 5d). Consistent with the remote contextual recall results, TSPAN7-cKO mice and mice expressing TSPAN7 P172H showed reduced Homer1/VGLUT1-positive synapse density in the BLA after context + cue recall, whereas VGLUT1-positive presynaptic bouton volume remained comparable across genotypes and conditions (Extended Data Fig. 5e–g). Finally, we examined whether TSPAN7 is required for behaviourally reactivated synaptic contacts by applying doxycycline-gated dual-eGRASP to the mPFC–BLA pathway under the context + cue recall condition after fear conditioning. In this assay, "E" denotes reactivated neurons and "N" denotes non-reactivated neurons, such that EE synapses represent contacts between reactivated prefrontal and amygdala ensembles. Before conditioning, CFP reporter density was comparable across control, TSPAN7-cKO and TSPAN7 P172H groups, indicating that the eGRASP signal was not confounded by differences in reporter expression (Extended Data Fig. 5h,i). After context + cue recall, NN and NE synapse densities were largely unchanged across genotypes, whereas EE synapse density was increased relative to EN synapses in control mice (Extended Data Fig. 5h,j). This recall-associated increase in EE synapses was markedly reduced in TSPAN7-cKO mice and was similarly impaired by expression of the disease-linked TSPAN7 P172H variant, with EE synapse density remaining comparable to EN synapses in both TSPAN7-perturbed groups (Extended Data Fig. 5h,k). In addition, CFP- and YFP-positive puncta volumes were comparable across genotypes, consistent with the unchanged VGLUT1-positive bouton volume observed in the anatomical synapse analysis (Extended Data Fig. 5l,m). Together, these results indicate that TSPAN7 is required for contextual recall-associated strengthening of synaptic connectivity between reactivated mPFC and BLA ensembles.

*Proximity proteomics identifies CPLX2 as a TSPAN7-linked presynaptic effector*

To elucidate how TSPAN7 regulates recall-activated synaptic remodelling, we sought to identify TSPAN7-associated proteins in the immediate presynaptic vicinity. We generated a TurboID fusion construct of TSPAN7 (TSPAN7–TurboID) and verified its proximity-labelling activity in cultured neurons (Fig. 4a and Extended Data Fig. 6a,b). We applied TSPAN7–TurboID *in vivo* to profile the TSPAN7-proximal presynaptic proteome in the mPFC–BLA

pathway (Fig. 4b)[28,31]. After confirming robust streptavidin labelling in the BLA following AAV-mediated expression of TSPAN7–TurboID in PrL neurons (Extended Data Fig. 6c), we microdissected the BLA and subjected streptavidin-enriched biotinylated proteins to quantitative LC–MS/MS. This analysis identified 66 proteins enriched in TSPAN7–TurboID samples relative to controls (Extended Data Fig. 6d; $\log_2FC > 2$, $P < 0.05$; Supplementary Table 4). GO enrichment analysis and protein–protein interaction networks showed strong enrichment for vesicle-mediated transport and synaptic signalling, especially SNARE complex proteins (Fig. 4c, Extended Data Fig. 6d,e, Supplementary Tables 5 and 6). Among the enriched candidates, we focused on complexin-2 (CPLX2), a SNARE-binding protein that modulates synaptic vesicle fusion and is implicated in major depression and schizophrenia[49,50]. CPLX2 was recovered in streptavidin pull-downs of TSPAN7–TurboID-expressing cultured neurons (Extended Data Fig. 6f and g). In brain sections, TSPAN7–TurboID-driven streptavidin-positive puncta co-localised with endogenous CPLX2 in the BLA (Extended Data Fig. 6h), indicating that CPLX2 resides near TSPAN7 at presynaptic release sites in the mPFC−BLA pathway. These results nominated CPLX2 as a prominent TSPAN7-linked presynaptic candidate in the mPFC–BLA pathway.

*TSPAN7–CPLX2 signalling drives presynaptic remodelling during remote contextual recall*

Next, we investigated how TSPAN7 controls presynaptic remodelling at recall-engaged synapses. Because TSPAN7 accumulated at mPFC–BLA synapses during remote contextual recall and was required for recall-associated synapse organization, we asked whether it regulates presynaptic release machinery through interaction with CPLX2, a synaptic vesicle-associated regulator of SNARE complex function. In cultured neurons, TSPAN7 and CPLX2 partially overlapped within VGLUT1-positive boutons under basal conditions (Extended Data Fig. 7a–d). High-potassium depolarisation increased the density of TSPAN7/CPLX2 double-positive puncta at VGLUT1-positive terminals, indicating activity-dependent co-recruitment of these proteins to excitatory presynaptic boutons (Extended Data Fig. 7a–d). This depolarisation-induced co-accumulation was abolished by expression of the disease-linked TSPAN7 P172H variant (Extended Data Fig. 7a–d). Co-immunoprecipitation assays further supported activity-dependent complex formation between TSPAN7 and CPLX2. Minimal CPLX2 co-immunoprecipitated with TSPAN7 under basal conditions, whereas high-potassium stimulation increased TSPAN7–CPLX2 co-immunoprecipitation (Extended Data Fig. 7e,f). This activity-dependent association was abolished by TSPAN7 P172H expression (Extended

Data Fig. 7e,f), indicating that neuronal activity promotes TSPAN7–CPLX2 complex assembly and that the P172H mutation disrupts this process. We next asked whether TSPAN7–CPLX2 signalling promotes assembly of the presynaptic SNARE machinery. After high-potassium stimulation, SDS-resistant SNARE complexes were isolated from cultured neurons. Depolarisation increased SNARE complex abundance in neurons co-expressing TSPAN7 and CPLX2 compared with controls (Extended Data Fig. 7g,h). TSPAN7 knockout reduced depolarisation-induced SNARE complex assembly, and TSPAN7 P172H failed to rescue this deficit (Extended Data Fig. 7i,j). CPLX2 deletion phenocopied TSPAN7 loss, and combined depletion of TSPAN7 and CPLX2 did not further decrease SNARE complex levels (Extended Data Fig. 7i,j), indicating that TSPAN7 and CPLX2 act in a common pathway to promote activity-dependent SNARE assembly. We then examined whether this pathway supports activity-induced synaptic vesicle recycling. Vesicle exo-endocytosis was measured using a luminal Synaptotagmin 1 antibody uptake assay (Extended Data Fig. 7k). In control neurons, high-potassium stimulation induced robust Synaptotagmin 1 uptake into VGLUT1-positive boutons, reflecting efficient synaptic vesicle recycling (Extended Data Fig. 7l,m). TSPAN7 knockout reduced high-potassium-induced Synaptotagmin 1 uptake, and this impairment was not rescued by TSPAN7 P172H expression (Extended Data Fig. 7l,m). CPLX2 deletion caused a similar reduction in Synaptotagmin 1 internalisation and responsive boutons, and combined TSPAN7/CPLX2 loss did not further exacerbate these defects (Extended Data Fig. 7l,m). These results indicate that TSPAN7 and CPLX2 function in a common presynaptic pathway that couples neuronal activity to SNARE complex assembly and synaptic vesicle recycling.

Building on these mechanistic findings, we next tested whether TSPAN7-dependent CPLX2 recruitment occurs at mPFC–BLA synapses during remote contextual recall *in vivo* (Fig. 4d). STED imaging revealed that FR-L increased CPLX2 accumulation in mCherry-positive mPFC–BLA boutons compared with NF controls (Fig. 4e,f). This recall-associated CPLX2 accumulation was absent in TSPAN7-cKO mice and was similarly impaired by TSPAN7 P172H expression (Fig. 4e,f), indicating that TSPAN7 function is required for recall-associated CPLX2 recruitment to mPFC–BLA presynaptic terminals during remote contextual recall. We next asked whether remote contextual recall also remodels SNAP25-positive release sites at mPFC–BLA synapses and whether this process depends on TSPAN7–CPLX2 signalling (Fig. 4d). STED imaging showed that FR-L increased the mean SNAP25 signal at release sites within VGLUT1-positive boutons in the BLA compared with NF controls, consistent with presynaptic release-site remodelling during remote contextual recall (Fig. 4g,h)[51,52]. This FR-L-induced enhancement of SNAP25-positive release sites was absent in

TSPAN7-cKO mice. The same recall-associated increase was also lost in TSPAN7 P172H mice, CPLX2-cKO mice and mice lacking both TSPAN7 and CPLX2 (Fig. 4g,h), indicating that TSPAN7–CPLX2 signalling is required for recall-associated release-site remodelling in the mPFC–BLA pathway. Consistent with these contextual recall results, analyses under the context + cue recall condition used for the initial ActProX-ID screen showed similar presynaptic remodelling at recall-engaged mPFC–BLA synapses (Extended Data Fig. 8c-h; Supplementary Table 1). Dual-eGRASP analysis revealed that yellow-labelled reactivated synapses contained more SNAP25 puncta per bouton than cyan-labelled non-reactivated synapses (Extended Data Fig. 8a,b). STED analysis further showed increased presynaptic CPLX2 accumulation and enhanced SNAP25-positive release-site features at recall-engaged synapses under this condition (Extended Data Fig. 8c–h). Thus, the presynaptic remodelling observed during remote contextual recall was also detectable under the context + cue recall condition. Finally, we assessed whether disruption of TSPAN7 affects synaptic transmission in the mPFC–BLA circuit. Whole-cell recordings from BLA pyramidal neurons showed that the frequency and amplitude of spontaneous EPSCs were comparable across genotypes, indicating preserved basal excitatory synaptic drive (Extended Data Fig. 8i–k). In contrast, optogenetic activation of mPFC–BLA projections expressing hChR2(H134R) revealed an increased paired-pulse ratio in TSPAN7-cKO and TSPAN7 P172H mice relative to controls (Fig. 4i–k), indicating reduced presynaptic release probability at mPFC–BLA synapses. Together, these findings show that activity-dependent TSPAN7–CPLX2 signalling promotes presynaptic remodelling by driving CPLX2 recruitment, SNARE complex assembly and SNAP25-positive release-site organisation. This pathway supports efficient synaptic vesicle recycling and presynaptic release efficacy at recall-engaged mPFC–BLA synapses during remote contextual recall.

*TSPAN7-dependent presynaptic organisation supports remote contextual memory*

Having identified TSPAN7 as a presynaptic component recruited to recall-activated mPFC–BLA synapses and as a CPLX2 partner that promotes presynaptic SNARE assembly, vesicle recycling and excitatory–excitatory connectivity (Figs. 3 and 4), we next asked whether TSPAN7-dependent presynaptic remodelling is required for memory functions supported by the mPFC–BLA pathway. Because remote contextual fear recall engages hippocampus–mPFC–BLA interactions, whereas tone-cued fear is mediated primarily by thalamic and auditory cortical inputs to the BLA with more limited prefrontal involvement[7,53–55], we directly compared the contribution of TSPAN7 to these distinct forms of fear memory. TSPAN7-cKO

and TSPAN7 P172H mutant mice underwent fear conditioning and were tested for recent and remote memory (Fig. 4l). Acquisition during training, including baseline and post-shock freezing, was indistinguishable among genotypes (Extended Data Fig. 9a–c), indicating intact learning. In addition, both recent and remote tone-cued freezing were comparable across genotypes, indicating preserved cued fear memory expression (Fig. 4n,p and Extended Data Fig. 9d,e). Contextual freezing was also unchanged at the recent time point (Fig. 4m), but was significantly reduced during remote contextual recall in TSPAN7-cKO and TSPAN7 P172H mice compared with controls (Fig. 4o). These findings indicate that TSPAN7 disruption preferentially impairs remote contextual fear recall, consistent with our observation that TSPAN7 localises to recall-reactivated mPFC–BLA synaptic contacts and supports synapse formation and presynaptic organisation in this pathway (Figs. 3 and 4).

Given the genetic association of TSPAN7 and CPLX2 with neurodevelopmental disorders involving altered locomotor activity, anxiety-related behaviour and social dysfunction[41,56,57], we next profiled these behavioural domains in the same cohort. In the open-field test (OFT), TSPAN7-cKO mice did not differ significantly from controls in total distance travelled, centre-zone time, immobility time or mean velocity during mobile periods, although several measures showed nonsignificant trends towards increased locomotor activity and centre exploration (Extended Data Fig. 9f–j). By contrast, mice expressing the TSPAN7 P172H variant showed significantly increased total distance travelled, centre-zone time and mean velocity during mobile periods, together with reduced immobility time (Extended Data Fig. 9f–j), consistent with increased locomotor activity and centre exploration. In the elevated plus maze (EPM), time spent in the open arms, the number of open-arm entries and the ratio of open to total arm entries were comparable across genotypes (Extended Data Fig. 9k–o), indicating no detectable change in anxiety-like behaviour. We then examined social behaviour using the three-chamber test and separately quantified time spent in the cage-vicinity zone (“approach”) and in the sniffing zone (“direct contact”), because proximity-based measures do not necessarily distinguish social approach from direct social investigation (Extended Data Fig. 9p,q)[58–60]. All genotypes spent significantly more time in the cage-vicinity zone near the cage containing a novel conspecific than near the empty cage, and cage-vicinity preference scores were comparable across genotypes, indicating preserved social approach behaviour (Extended Data Fig. 9r,s). Similarly, all genotypes spent significantly more time in the sniffing zone near the novel conspecific than near the empty cage, and sniffing-zone preference scores were comparable across genotypes, indicating preserved direct social investigation at the group-preference level (Extended Data Fig. 9t,u). We next normalized sniffing-zone time to cage-

vicinity time to assess close investigation relative to approach behaviour. This sniffing/cage-vicinity ratio remained higher for the social target than for the empty cage across genotypes (Extended Data Fig. 9v). However, the overall sniffing/cage-vicinity social interaction ratio was significantly reduced in TSPAN7 P172H mice and showed a similar nonsignificant tendency in TSPAN7-cKO mice (Extended Data Fig. 9w). Thus, despite preserved fear acquisition, recent contextual recall and tone-cued recall, TSPAN7 functional perturbation preferentially impaired remote contextual fear recall. Together with the preceding synaptic analyses, these findings identify TSPAN7-dependent presynaptic organisation in the mPFC–BLA pathway as a critical mechanism supporting remote contextual memory recall.

## Discussion

Using ActProX-ID, a spatiotemporal strategy for presynaptic proteomic profiling in recall-captured mPFC–BLA projection neurons, we profiled presynaptically enriched proteomic states associated with recent and remote fear-memory recall (Figs. 1 and 2). This approach revealed that recall engages overlapping but phase-biased presynaptic protein programmes within a defined long-range pathway. The remote-recall condition was particularly associated with proteins involved in synaptic vesicle trafficking, which led us to identify a TSPAN7–CPLX2 module linking recall-associated presynaptic remodelling to SNARE complex assembly, synaptic vesicle cycling and presynaptic release efficacy (Figs. 3 and 4). Subsequent validation under remote contextual recall showed that disruption of TSPAN7 or the disease-linked P172H variant impaired remote contextual fear memory while sparing recent contextual and tone-cued fear memory (Fig. 4 and Extended Data Fig. 9). Thus, our study connects behaviourally recruited projection neurons to presynaptic molecular remodelling and identifies TSPAN7-dependent presynaptic organisation as a mechanism supporting remote contextual memory recall (Extended Data Fig. 10).

Activity-dependent tagging has enabled genetic access to neuronal populations recruited during learning and recall, and transcriptomic profiling of tagged or engram-related neurons has revealed molecular programmes associated with memory states[5,11–13]. However, these approaches do not directly resolve how recall-associated ensembles organise their output through the presynaptic terminals of defined long-range projections. This is an important distinction because communication through long-range projections is shaped locally at presynaptic boutons by synaptic vesicle cycling, release-site organisation and short-term release properties[16,17,61,62]. We previously developed ProX-ID to enable projection-targeted presynaptic proteomic profiling *in vivo*[33]. ActProX-ID extends this strategy by incorporating

TRAP2-dependent capture of recall-associated neuronal activity into the same presynaptic labelling framework.

ActProX-ID addresses an important methodological gap in synaptic proteomics by linking activity-dependent ensemble capture with projection-targeted presynaptic proteomic profiling *in vivo*[22,23]. Synaptosome-based methods, including fluorescence-activated synaptosome sorting, have provided powerful proteome-scale views of synapse-type diversity across brain regions and genetically labelled synaptic populations[63–65], whereas proximity-labelling approaches have enabled spatially restricted proteomic analyses of defined neuronal compartments, synaptic interfaces and glial–neuronal contact sites[28–31,66,67]. By adding activity-dependent genetic access to projection-targeted presynaptic proteomics, ActProX-ID profiles presynaptically enriched compartments of long-range projection neurons captured during recall-associated activity windows. Because TRAP2-dependent recombination and subsequent TurboID-mediated biotin labelling occur over time, ActProX-ID should not be interpreted as providing an instantaneous snapshot of protein composition at the exact moment of recall. Instead, it provides a presynaptically enriched proteomic readout from defined projection neurons genetically captured during recall-associated activity, thereby linking recall-associated neuronal recruitment to projection-level presynaptic molecular states. This interpretation is consistent with previous activity-dependent tagging studies showing that recall-associated prelimbic and mPFC ensembles can be reactivated during subsequent retrieval and contribute to remote memory expression[4,5,43]. Thus, ActProX-ID provides a framework for connecting behaviourally recruited projection neurons to presynaptic molecular states in defined long-range circuits.

Applying this framework to the mPFC–BLA pathway revealed recall-phase-biased organisation of the presynaptic proteome. Notably, proteins preferentially represented during recent recall were biased towards cytoskeletal organisation, synaptic organisation and cell projection morphogenesis, whereas proteins preferentially represented during remote recall were biased towards synaptic vesicle trafficking (Fig. 2 and Extended Data Fig. 2). These patterns suggest that presynaptic compartments in recall-captured mPFC–BLA projection neurons shift from structural and organisational remodelling during early recall towards enhanced synaptic vesicle cycling, release-site organisation and presynaptic release machinery during remote recall. The remote recall-associated presynaptic signature also showed concordance with gene-expression patterns in marmoset prefrontal neurons and included disease-linked proteins associated with behavioural domains relevant to socioemotional function, supporting the cross-species and disease relevance of this projection-resolved

presynaptic architecture (Fig. 2 and Extended Data Fig. 2). Together, these findings indicate that remote recall is associated with a distinct presynaptic molecular state in the mPFC–BLA pathway, marked by prominent engagement of synaptic vesicle trafficking.

TSPAN7 provides a mechanistic link between the remote recall-associated presynaptic programme identified by ActProX-ID and disease-relevant presynaptic remodelling in the mPFC–BLA pathway (Extended Data Fig. 10). TSPAN7 has been studied mainly as a postsynaptic tetraspanin involved in excitatory synapse development, spine maturation and AMPA receptor trafficking[41], and pathogenic variants in TSPAN7 cause X-linked intellectual disability and have been associated with autism spectrum disorder (ASD)[39,47,56]. Its identification in the ActProX-ID dataset therefore raised the possibility that a disease-linked molecule classically associated with postsynaptic development also contributes to activity-dependent presynaptic remodelling in long-range circuits. Consistent with this idea, endogenous TSPAN7 accumulated at mPFC–BLA presynaptic terminals during remote contextual recall and was associated with behaviourally re-engaged synaptic contacts under the context + cue recall condition (Fig. 3 and Extended Data Fig. 3). TSPAN7 disruption reduced recall-associated synaptic remodelling and ensemble–ensemble synaptic connectivity in the BLA while largely sparing excitatory synapse density within the mPFC. Moreover, the disease-linked P172H variant failed to rescue these defects despite preserved presynaptic localisation[68,69]. Together, these findings support a model in which TSPAN7 is required for recall-associated presynaptic remodelling in the mPFC–BLA pathway, and in which the disease-linked P172H variant uncouples preserved presynaptic localisation from presynaptic function, suggesting a presynaptic route through which pathogenic TSPAN7 variation may affect memory-relevant circuit function (Extended Data Fig. 10).

Mechanistically, our data identify CPLX2 as a TSPAN7-associated presynaptic effector of recall-associated remodelling (Fig. 4 and Extended Data Fig. 6–8). CPLX2 is a SNARE-binding protein that regulates synaptic vesicle fusion and has been linked to cognitive dysfunction in psychiatric disorders[57,70–72]. TSPAN7-proximal proteomics nominated CPLX2 as a candidate in the mPFC–BLA pathway, and loss of TSPAN7, expression of TSPAN7 P172H or loss of CPLX2 impaired stimulation-induced SNARE complex assembly and Synaptotagmin 1 uptake (Extended Data Fig. 7). These findings suggest that TSPAN7 and CPLX2 functionally converge on mechanisms supporting activity-evoked synaptic vesicle recycling. This interpretation is consistent with previous evidence that complexins regulate SNARE-dependent vesicle fusion and neurotransmitter release, and that CPLX2 perturbation affects cognitive and synaptic plasticity-related phenotypes[70,71,73–75]. It is also supported by

studies showing that hippocampal SNAP25-dependent vesicle-release machinery is required for long-term contextual fear memory and spatial memory, whereas short-term memory can remain intact[51,52]. Our findings extend these observations by placing CPLX2-dependent SNAP25-positive release-site organisation within recall-engaged mPFC–BLA boutons during remote contextual recall (Extended Data Fig. 10). *In vivo*, remote contextual recall increased CPLX2 accumulation and enhanced SNAP25-positive release-site organisation at mPFC–BLA boutons (Fig. 4). TSPAN7 disruption or expression of the disease-linked P172H variant abolished recall-associated CPLX2 recruitment. Consistent with a role for CPLX2 in recall-associated release-site remodelling, disruption of TSPAN7, expression of TSPAN7 P172H or loss of CPLX2 abolished the recall-induced enhancement of SNAP25-positive release-site organisation (Fig. 4). Behaviourally, TSPAN7-cKO and TSPAN7 P172H mice showed impaired remote contextual freezing, whereas acquisition, recent contextual freezing and tone-cued freezing were preserved (Fig. 4). Importantly, this remote contextual freezing deficit was observed in TSPAN7-cKO mice despite the absence of significant open-field hyperlocomotion, arguing against a simple explanation based on altered locomotor activity, impaired freezing expression or general behavioural performance. Thus, the TSPAN7–CPLX2 module links recall-associated presynaptic release-site organisation to remote contextual memory and reveals a disease-relevant presynaptic mechanism underlying memory-circuit dysfunction (Extended Data Fig. 10). Future studies should determine whether restoring CPLX2 recruitment or SNAP25-positive release-site organisation is sufficient to rescue TSPAN7-dependent remote-memory deficits, and whether similar presynaptic release-site programmes operate in other remote-memory circuits. Although our data do not establish that TSPAN7-dependent mPFC–BLA presynaptic remodelling directly mediates locomotor or social behaviour, mice expressing the disease-linked TSPAN7 P172H variant in mPFC neurons showed increased locomotor activity and a modest reduction in close social investigation relative to social approach, whereas TSPAN7-cKO mice showed only nonsignificant trends in these measures (Extended Data Fig. 9). Previous germline or whole-animal TSPAN7/Tm4sf2 knockout studies, distinct from our prefrontal neuron-restricted manipulation, reported broad neurodevelopmental phenotypes, including ASD-like and intellectual disability-like behaviours, altered sociability, repetitive behaviour and synaptic abnormalities[56,76]. Thus, while our data most directly support a role for TSPAN7-dependent presynaptic organisation in mPFC–BLA-dependent remote contextual recall, the P172H-associated behavioural changes are consistent with the broader disease relevance of TSPAN7 dysfunction and raise the possibility that prefrontal TSPAN7 perturbation contributes to vulnerability in socioemotional

circuit function. Overall, this study establishes ActProX-ID as a spatiotemporal presynaptic proteomic strategy that links behaviourally recruited projection neurons to presynaptic molecular remodelling, and identifies TSPAN7–CPLX2-dependent release-site organisation as a presynaptic mechanism supporting remote contextual memory recall.

**Acknowledgements**

We thank Y. Okugawa and R. Tamiya of the Life Science Unit, Technical Support Office, Division of Bioresource and Environmental Sciences, Research and Education Support Center, Faculty of Agriculture, Kyushu University, for expert assistance with STELLARIS STED microscopy, and T. Igarashi and T. Fukuda of Leica Microsystems for technical support. This work was supported by a Grant-in-Aid for Scientific Research B (21380936), PRESTO (21461219 and 24029397) from JST (T.T.), a Brain Mind 2.0 from AMED (JP23wm0625001 for T.S. and 24019272, 24019528 for T.T.), The Ono Pharmaceutical Foundation for Oncology (T.T.), Immunology and Neurology (T.T.), the Memorial Foundation for Medical and Pharmaceutical Research (T.T.), a Research Grant from the JGC Saneyoshi Scholarship Foundation (T.T.), the Takeda Science Foundation (T.T.) and a MEXT Grants-in-Aid for Scientific Research on Innovative Areas “Cell type census of adaptive neuronal circuits: biological mechanisms of structural and functional organization (Adaptive Circuit Census, ACC)” (24H01250) (T. T.). This work was also supported by the Medical Research Center Initiative for High Depth Omics (H.K. and T.T.) and Joint Usage and Joint Research Programs of the Institute of Advanced Medical Sciences, Tokushima University (T.T.).

**Author contributions**

S.N., Y. Ito and T.T. conceived and designed the study. S.N., Y. Ito, A. Fukuda, J.M., S.M., H.K. and T.T. wrote the manuscript. S.N., M.F. and T.T. generated the constructs. S.N., Y. Ito, H.K. and T.T. performed and analysed the *in vivo* BioID-based proteomics experiments. K.O. and T.S. performed the spatial transcriptomic analysis of marmoset brains. S.N., J.M., A.I., S.H.S. and T.T. performed biological experiments. S.N., J.M., M.F., A. Fujisaki and T.T. performed imaging and morphological analyses. S.M. and H.T. performed electrophysiological analyses, under the supervision from Y. Ikegaya. Y. Ito and A. Fukuda performed behavioural analyses. T.T. supervised the project and acquired funding. All authors discussed the results and commented on the manuscript.

**Data availability**

The MS proteomics data have been deposited to the ProteomeXchange Consortium via the jPOST partner repository with the dataset identifiers PXD072691 (ActProX-ID), PXD072692 (ProX-ID), and PXD072696 (TSPAN7-TurboID). During peer review, the datasets have been made available to the reviewers via private preview links.

**Code availability**

No custom code central to the main claims of this study was generated. All proteomic and bioinformatic analyses were performed using publicly available software with default or specified parameters as described in the Methods. The software used in this study includes DIA-NN 1.8.1, Perseus 2.0.1.1, Metascape (https://metascape.org), Cytoscape 3.10.3 [28,31] with the stringApp (v2.2.0) plugin, MATLAB R2024a (MathWorks), R 4.4.1 with the Seurat (v5.3.0), Harmony and R 4.5.0 with synaptome.db packages. Analysis scripts used to generate the figures are available from the corresponding author upon reasonable request.

**Additional information**

Correspondence and requests for materials should be addressed to T.T. (E-mail: tetsuya.takano@bioreg.kyushu-u.ac.jp).

**Conflict of interest**

The authors declare no competing financial interests.

## References


1. Tonegawa, S., Liu, X., Ramirez, S. & Redondo, R. Memory engram cells have come of age. *Neuron* **87**, 918–931 (2015).
2. Josselyn, S. A. & Tonegawa, S. Memory engrams: Recalling the past and imagining the future. *Science* **367**, eaaw4325 (2020).
3. Choi, J.-H. *et al.* Interregional synaptic maps among engram cells underlie memory formation. *Science* **360**, 430–435 (2018).
4. Kitamura, T. *et al.* Engrams and circuits crucial for systems consolidation of a memory. *Science* **356**, 73–78 (2017).
5. DeNardo, L. A. *et al.* Temporal evolution of cortical ensembles promoting remote memory retrieval. *Nat. Neurosci.* **22**, 460–469 (2019).
6. Matos, M. R. *et al.* Memory strength gates the involvement of a CREB-dependent cortical fear engram in remote memory. *Nat. Commun.* **10**, 2315 (2019).
7. Maren, S., Phan, K. L. & Liberzon, I. The contextual brain: implications for fear conditioning, extinction and psychopathology. *Nat. Rev. Neurosci.* **14**, 417–428 (2013).
8. Zelikowsky, M., Hersman, S., Chawla, M. K., Barnes, C. A. & Fanselow, M. S. Neuronal ensembles in amygdala, hippocampus, and prefrontal cortex track differential components of contextual fear. *J. Neurosci.* **34**, 8462–8466 (2014).
9. Arruda-Carvalho, M. & Clem, R. L. Pathway-selective adjustment of prefrontal-amygdala transmission during fear encoding. *J. Neurosci.* **34**, 15601–15609 (2014).
10. McGarry, L. M. & Carter, A. G. Prefrontal cortex drives distinct projection neurons in the basolateral amygdala. *Cell Rep.* **21**, 1426–1433 (2017).
11. Guenthner, C. J., Miyamichi, K., Yang, H. H., Heller, H. C. & Luo, L. Permanent genetic access to transiently active neurons via TRAP: targeted recombination in active populations. *Neuron* **78**, 773–784 (2013).
12. Rao-Ruiz, P. *et al.* Engram-specific transcriptome profiling of contextual memory consolidation. *Nat. Commun.* **10**, 2232 (2019).
13. Chen, M. B., Jiang, X., Quake, S. R. & Südhof, T. C. Persistent transcriptional programmes are associated with remote memory. *Nature* **587**, 437–442 (2020).
14. Marco, A. *et al.* Mapping the epigenomic and transcriptomic interplay during memory formation and recall in the hippocampal engram ensemble. *Nat. Neurosci.* **23**, 1606–1617 (2020).
15. Sun, W. *et al.* Spatial transcriptomics reveal neuron-astrocyte synergy in long-term memory. *Nature* **627**, 374–381 (2024).

16. Südhof, T. C. The presynaptic active zone. *Neuron* **75**, 11–25 (2012).
17. Regehr, W. G. Short-term presynaptic plasticity. *Cold Spring Harb. Perspect. Biol.* **4**, a005702 (2012).
18. Holt, C. E. & Schuman, E. M. The central dogma decentralized: new perspectives on RNA function and local translation in neurons. *Neuron* **80**, 648–657 (2013).
19. Holt, C. E., Martin, K. C. & Schuman, E. M. Local translation in neurons: visualization and function. *Nat. Struct. Mol. Biol.* **26**, 557–566 (2019).
20. Hafner, A.-S., Donlin-Asp, P. G., Leitch, B., Herzog, E. & Schuman, E. M. Local protein synthesis is a ubiquitous feature of neuronal pre- and postsynaptic compartments. *Science* **364**, eaau3644 (2019).
21. Li, L., Yu, J. & Ji, S.-J. Axonal mRNA localization and translation: local events with broad roles. *Cell. Mol. Life Sci.* **78**, 7379–7395 (2021).
22. Ito, Y., Nagamoto, S. & Takano, T. Synaptic proteomics decode novel molecular landscape in the brain. *Front. Mol. Neurosci.* **17**, 1361956 (2024).
23. Matsubayashi, J. & Takano, T. Proximity labeling uncovers the synaptic proteome under physiological and pathological conditions. *Front. Cell. Neurosci.* **19**, 1638627 (2025).
24. Roux, K. J., Kim, D. I., Raida, M. & Burke, B. A promiscuous biotin ligase fusion protein identifies proximal and interacting proteins in mammalian cells. *J. Cell Biol.* **196**, 801–810 (2012).
25. Branon, T. C. *et al.* Efficient proximity labeling in living cells and organisms with TurboID. *Nat. Biotechnol.* **36**, 880–887 (2018).
26. Rhee, H.-W. *et al.* Proteomic mapping of mitochondria in living cells via spatially restricted enzymatic tagging. *Science* **339**, 1328–1331 (2013).
27. Lam, S. S. *et al.* Directed evolution of APEX2 for electron microscopy and proximity labeling. *Nat. Methods* **12**, 51–54 (2015).
28. Uezu, A. *et al.* Identification of an elaborate complex mediating postsynaptic inhibition. *Science* **353**, 1123–1129 (2016).
29. Loh, K. H. *et al.* Proteomic Analysis of Unbounded Cellular Compartments: Synaptic Clefts. *Cell* **166**, 1295-1307.e21 (2016).
30. Cijsouw, T. *et al.* Mapping the Proteome of the Synaptic Cleft through Proximity Labeling Reveals New Cleft Proteins. *Proteomes* **6**, (2018).
31. Takano, T. *et al.* Chemico-genetic discovery of astrocytic control of inhibition in vivo. *Nature* **588**, 296–302 (2020).

32. Takano, T. & Soderling, S. H. Tripartite synaptomics: Cell-surface proximity labeling in vivo. *Neurosci. Res.* **173**, 14–21 (2021).
33. Ito, Y. *et al.* Spatial proteomics reveals prefrontal circuit diversity in socioemotional behaviour. *bioRxiv* (2026) doi:10.64898/2026.02.08.704617.
34. Koopmans, F. *et al.* SynGO: An evidence-based, expert-curated knowledge base for the synapse. *Neuron* **103**, 217-234.e4 (2019).
35. Niswender, C. M. & Conn, P. J. Metabotropic glutamate receptors: physiology, pharmacology, and disease. *Annu. Rev. Pharmacol. Toxicol.* **50**, 295–322 (2010).
36. Banerjee, A., Larsen, R. S., Philpot, B. D. & Paulsen, O. Roles of presynaptic NMDA receptors in neurotransmission and plasticity. *Trends Neurosci.* **39**, 26–39 (2016).
37. Schenk, U. & Matteoli, M. Presynaptic AMPA receptors: more than just ion channels? *Biol. Cell* **96**, 257–260 (2004).
38. Sorokina, O., Sorokin, A. & Armstrong, J. D. Synaptome.db: a bioconductor package for synaptic proteomics data. *Bioinform. Adv.* **2**, vbac086 (2022).
39. Zemni, R. *et al.* A new gene involved in X-linked mental retardation identified by analysis of an X;2 balanced translocation. *Nat. Genet.* **24**, 167–170 (2000).
40. Abidi, F. E. A novel 2 bp deletion in the TM4SF2 gene is associated with X-linked mental retardation in a large MRX family. *J Med Genet* **39**, 430–434 (2002).
41. Bassani, S. *et al.* The X-linked intellectual disability protein TSPAN7 regulates excitatory synapse development and AMPAR trafficking. *Neuron* **73**, 1143–1158 (2012).
42. Boda, B., Mas, C. & Muller, D. Activity-dependent regulation of genes implicated in X-linked non-specific mental retardation. *Neuroscience* **114**, 13–17 (2002).
43. Lee, J.-H., Kim, W. B., Park, E. H. & Cho, J.-H. Neocortical synaptic engrams for remote contextual memories. *Nat. Neurosci.* **26**, 259–273 (2023).
44. Gao, Y. *et al.* Plug-and-play protein modification using homology-independent universal genome engineering. *Neuron* **103**, 583-597.e8 (2019).
45. Gao, Y. *et al.* Proximity analysis of native proteomes reveals phenotypic modifiers in a mouse model of autism and related neurodevelopmental conditions. *Nat. Commun.* **15**, (2024).
46. Kim, J.-I., Choi, D. I. & Kaang, B.-K. Strengthened connections between engrams encode specific memories. *BMB Rep.* **51**, 369–370 (2018).
47. Noor, A. *et al.* Copy number variation analysis and sequencing of the X-linked mental retardation gene TSPAN7/TM4SF2 in patients with autism spectrum disorder. *Psychiatr. Genet.* **19**, 154–155 (2009).

48. Piton, A. *et al.* Systematic resequencing of X-chromosome synaptic genes in autism spectrum disorder and schizophrenia. *Mol. Psychiatry* **16**, 867–880 (2011).
49. Eastwood, S. L. & Harrison, P. J. Hippocampal synaptic pathology in schizophrenia, bipolar disorder and major depression: a study of complexin mRNAs. *Mol. Psychiatry* **5**, 425–432 (2000).
50. Glantz, L. A. & Lewis, D. A. Decreased dendritic spine density on prefrontal cortical pyramidal neurons in schizophrenia. *Arch. Gen. Psychiatry* **57**, 65–73 (2000).
51. Hou, Q. *et al.* SNAP-25 in hippocampal CA1 region is involved in memory consolidation. *Eur. J. Neurosci.* **20**, 1593–1603 (2004).
52. Hou, Q.-L. *et al.* SNAP-25 in hippocampal CA3 region is required for long-term memory formation. *Biochem. Biophys. Res. Commun.* **347**, 955–962 (2006).
53. Liu, W.-Z. *et al.* Identification of a prefrontal cortex-to-amygdala pathway for chronic stress-induced anxiety. *Nat. Commun.* **11**, 2221 (2020).
54. Kim, S. *et al.* Neural circuit pathology driven by Shank3 mutation disrupts social behaviors. *Cell Rep.* **39**, 110906 (2022).
55. Boatman, J. A. & Kim, J. J. A thalamo-cortico-amygdala pathway mediates auditory fear conditioning in the intact brain. *Eur. J. Neurosci.* **24**, 894–900 (2006).
56. Pang, S. *et al.* Integrin β1/FAK/SRC signal pathway is involved in autism spectrum disorder in Tspan7 knockout rats. *Life Sci Alliance* **6**, (2023).
57. Begemann, M. *et al.* Modification of cognitive performance in schizophrenia by complexin 2 gene polymorphisms. *Arch. Gen. Psychiatry* **67**, 879–888 (2010).
58. Nadler, J. J. *et al.* Automated apparatus for quantitation of social approach behaviors in mice. *Genes Brain Behav.* **3**, 303–314 (2004).
59. Yang, M., Silverman, J. L. & Crawley, J. N. Automated three-chambered social approach task for mice. *Curr. Protoc. Neurosci.* **Chapter 8**, Unit 8.26 (2011).
60. Rein, B., Ma, K. & Yan, Z. A standardized social preference protocol for measuring social deficits in mouse models of autism. *Nat. Protoc.* **15**, 3464–3477 (2020).
61. Emperador-Melero, J. & Kaeser, P. S. Assembly of the presynaptic active zone. *Curr. Opin. Neurobiol.* **63**, 95–103 (2020).
62. Walter, A. M., Böhme, M. A. & Sigrist, S. J. Vesicle release site organization at synaptic active zones. *Neurosci. Res.* **127**, 3–13 (2018).
63. Biesemann, C. *et al.* Proteomic screening of glutamatergic mouse brain synaptosomes isolated by fluorescence activated sorting. *EMBO J.* **33**, 157–170 (2014).

64. van Oostrum, M. *et al.* The proteomic landscape of synaptic diversity across brain regions and cell types. *Cell* **186**, 5411-5427.e23 (2023).
65. Paget-Blanc, V. *et al.* A synaptomic analysis reveals dopamine hub synapses in the mouse striatum. *Nat. Commun.* **13**, 3102 (2022).
66. Dumrongprechachan, V. *et al.* Cell-type and subcellular compartment-specific APEX2 proximity labeling reveals activity-dependent nuclear proteome dynamics in the striatum. *Nat. Commun.* **12**, 4855 (2021).
67. Hobson, B. D. *et al.* Subcellular proteomics of dopamine neurons in the mouse brain. *Elife* **11**, (2022).
68. Gomot, M. *et al.* TM4SF2 gene involvement reconsidered in an XLMR family after neuropsychological assessment. *Am. J. Med. Genet.* **112**, 400–404 (2002).
69. Maranduba, C. M. da C. *et al.* Does the P172H mutation at the TM4SF2 gene cause X-linked mental retardation? *Am. J. Med. Genet. A* **124A**, 413–415 (2004).
70. Xue, M. *et al.* Complexins facilitate neurotransmitter release at excitatory and inhibitory synapses in mammalian central nervous system. *Proc. Natl. Acad. Sci. U. S. A.* **105**, 7875–7880 (2008).
71. Maximov, A., Tang, J., Yang, X., Pang, Z. P. & Südhof, T. C. Complexin controls the force transfer from SNARE complexes to membranes in fusion. *Science* **323**, 516–521 (2009).
72. Hass, J. *et al.* Complexin2 modulates working memory-related neural activity in patients with schizophrenia. *Eur. Arch. Psychiatry Clin. Neurosci.* **265**, 137–145 (2015).
73. Glynn, D. *et al.* Clorgyline-mediated reversal of neurological deficits in a Complexin 2 knockout mouse. *Hum. Mol. Genet.* **19**, 3402–3412 (2010).
74. Glynn, D., Bortnick, R. A. & Morton, A. J. Complexin II is essential for normal neurological function in mice. *Hum. Mol. Genet.* **12**, 2431–2448 (2003).
75. Yamauchi, Y. *et al.* Vulnerability of synaptic plasticity in the complexin II knockout mouse to maternal deprivation stress. *Brain Res.* **1056**, 59–67 (2005).
76. Murru, L. *et al.*Pharmacological Modulation of AMPAR Rescues Intellectual Disability-Like Phenotype in Tm4sf2−/y Mice. *Cereb Cortex*. 27(11):5369-5384 (2017).
77. Matsubayashi, J., Kawaguchi, Y., Kawakami, Y. & Takei, K. Brain-derived neurotrophic factor (BDNF) induces antagonistic action to Nogo signaling by the upregulation of lateral olfactory tract usher substance (LOTUS) expression. *J. Neurochem.* **164**, 29–43 (2023).

78. Savage, J. T. *et al.* SynBot is an open-source image analysis software for automated quantification of synapses. *Cell Rep. Methods* **4**, 100861 (2024).
79. Takano, T. *et al.* Discovery of long-range inhibitory signaling to ensure single axon formation. *Nat. Commun.* **8**, 33 (2017).
80. Doncheva, N. T. *et al.* Cytoscape stringApp 2.0: Analysis and visualization of heterogeneous biological networks. *J. Proteome Res.* **22**, 637–646 (2023).
81. Kanehisa, M., Furumichi, M., Sato, Y., Matsuura, Y. & Ishiguro-Watanabe, M. KEGG: biological systems database as a model of the real world. *Nucleic Acids Res.* **53**, D672–D677 (2025).
82. Kanehisa, M. Toward understanding the origin and evolution of cellular organisms. *Protein Sci.* **28**, 1947–1951 (2019).
83. Kanehisa, M. & Goto, S. KEGG: kyoto encyclopedia of genes and genomes. *Nucleic Acids Res.* **28**, 27–30 (2000).
84. Doncheva, N. T., Morris, J. H., Gorodkin, J. & Jensen, L. J. Cytoscape StringApp: Network analysis and visualization of proteomics data. *J. Proteome Res.* **18**, 623−632 (2019).
85. Shimogori, T., Onishi, K., Hoshino, T. & Nakanishi, M. Molecular architecture of primate specific neural circuit formation. *Res. Sq.* (2024) doi:10.21203/rs.3.rs-4082064/v1.
86. Hao, Y. *et al.* Dictionary learning for integrative, multimodal and scalable single-cell analysis. *Nat. Biotechnol.* **42**, 293–304 (2024).
87. Korsunsky, I. *et al.* Fast, sensitive and accurate integration of single-cell data with Harmony. *Nat. Methods* **16**, 1289–1296 (2019).
88. Yoshimoto, A., Morikawa, S., Kato, E., Takeuchi, H. & Ikegaya, Y. Top-down brain circuits for operant bradycardia. *Science* **384**, 1361–1368 (2024).

## Methods

### *Animals*

All animal experiments were conducted in accordance with the National Institutes of Health Guide for the Care and Use of Laboratory Animals and were approved by the Kyushu University Animal Experiment Committee (A24-335-1). Mice were housed in a specific pathogen-free animal facility with *ad libitum* access to food and water, maintained on a 12-h light/dark cycle. For *in vivo* studies, STOCK Fos$^{tm2.1(icre/ERT2)Luo}$/J mice (TRAP2 mice, Jackson Laboratory), Gt(ROSA)26Sor$^{tm1(CAG-cas9*,-EGFP)Fezh}$ mice (SpCas9 mice, Jackson Laboratory) or

wild-type (WT) C57BL/6J mice (Jackson Laboratory Japan) were used. Stereotaxic injections were performed in mice at the ages specified for each experiment. For behavioural experiments, both male and female mice were used. Experimental data were collected from mice aged 9–14 weeks. Mice were excluded from analysis if *post hoc* histology revealed off-target injections, unilateral expression, or insufficient expression in the target area.

***Plasmid construction***

V5-TurboID-NES_pcDNA3 (Addgene plasmid #107169; gift from Alice Ting) was used as the source of the TurboID coding sequence. ActProX-ID was first generated by subcloning the TurboID fragment together with GAP43 palmitoylation sites into a pAAV-CaMKII-ProX-ID backbone, and the resulting ActProX-ID cassette was then inserted into a pAAV-CaMKII-DIO backbone to generate pAAV-CaMKII-DIO-ActProX-ID. Axon-mCherry was amplified from pAAV-CaMKII-Axon-mCherry and subcloned into the pAAV-CAG-DIO vector. HiUGE vectors were used as previously described[44], and sgRNA sequences targeting TSPAN7 were designed using CRISPOR. The sequences used for HiUGE knock-in were as follows: HiUGE sgRNA#1, 5′-CCTGTTGGCCGTTGGAGTCT-3′, HiUGE sgRNA#2, 5′-CTGTTGGCCGTTGGAGTCTG-3′, HiUGE sgRNA#3, 5′-TGGATTTGTGTTTCGTCATG-3′. The HiUGE donor was designed to insert a V5 epitope into the C-terminal intracellular region of endogenous *Tspan7*. The insertion site was selected to avoid disruption of the transmembrane domains and C-terminal PDZ-binding motifs. Correct in-frame insertion was validated by sequencing and by immunostaining and immunoblotting for V5-tagged TSPAN7. pSpCas9(BB)-2A-GFP (PX458) was a gift from Feng Zhang (Addgene plasmid #48138). pAAV-TIWB-myrmScarlet-I-P2A-post-eGRASP (Addgene plasmid #111584), pAAV-EWB-DIO-myriRFP670V5-P2A-post-eGRASP (Addgene plasmid #111585), pAAV-EWB-DIO-cyan pre-eGRASP(p32) (Addgene plasmid #111589), pAAV-TIWB-yellow pre-eGRASP(p30) (Addgene plasmid #111588) and pAAV-FAH-rtTA3G (Addgene plasmid #120309) were gifts from Bong-Kiun Kaang. pAAV-CaMKII-Cre was a gift from Janelia Viral Tools (Addgene plasmid #182736). pAAV-EF1a-DIO-hChR2(H134R)-P2A-EYFP was a gift from Mingshan Xue (Addgene plasmid #139283). pAAV-pMecp2-SpCas9-spA (PX551) (Addgene plasmid #60957) and PX552 (pAAV-U6-sgRNA (SapI)_hSyn-GFP-KASH-bGH) (Addgene plasmid #60958) were gifts from Feng Zhang. pAAV-U6-sgRNA-hSyn-mCherry vectors were used as previously described[33], and sgRNA sequences targeting TSPAN7 and CPLX2 were designed using CRISPOR. The sequences used for knockout were as follows:

Scramble sgRNAs, 5′-GCGATCCCATGCCCTTAGAA-3′, 5′-GCGACCTCCCACGCAAGAAA-3′, 5′-GGCGCAACCGGCAATAGAGA-3′; TSPAN7 sgRNAs, 5′-GGGGTGATCCTGTTGGCCGT-3′, 5′-CTACATGCCGTGGTAGTCCA-3′, 5′-GCGTGCAGAACTACACCAAC-3′; CPLX2 sgRNAs, 5′-CAAGGCGAAACACGCCCGCA-3′, 5′-CATGGAAGCCGAGCGCGAGA-3′, 5′-AGCAGATCCGAGACAAGTAT-3′. Human TSPAN7 (wild-type), TSPAN7 P172H and CPLX2 coding sequences were synthesised and subcloned into the pAAV-CaMKII-MCS vector to generate pAAV-CaMKII-hTSPAN7, pAAV-CaMKII-hTSPAN7(P172H) and pAAV-CaMKII-CPLX2, respectively. The TSPAN7–TurboID expression construct (pAAV-CaMKII-TSPAN7-TurboID) was generated by synthesising the human TSPAN7 coding sequence and amplifying the TurboID fragment from V5-TurboID-NES_pcDNA3 (Addgene plasmid #107169), followed by in-frame fusion and subcloning into the pAAV-CaMKII-MCS vector. All constructs were confirmed by DNA sequencing. All primers are shown in Supplementary Table 7.

***Antibodies***

The following antibodies were used: rabbit anti-HA (Cell Signaling Technology, C29F4), rabbit anti-Homer1 (Synaptic Systems, 160-003), guinea pig anti-VGLUT-1 (Synaptic Systems, 135-304), mouse anti-α-Tubulin (Santa Cruz, sc-32293), rabbit anti-TSPAN7 (Invitrogen, PA576938), rat anti-HA (Roche/Sigma, 11867423001), mouse anti-HA (BioLegend, MMS-101P), mouse anti-Myc (CST, 2276), rabbit anti-CPLX2 (SYSY, 122102), rabbit anti-SNAP25 (Abcam, Ab41455), mouse anti-Synaptotagmin1 (SYSY, 105103), mouse anti-V5 (Invitrogen, R96025), rabbit anti-mCherry (Abcam, ab167453), chicken anti-GFP (Merck, AB16901), Alexa Fluor 488 Goat anti-Mouse IgG (ThermoFisher, A32723), Alexa Fluor 488 Goat anti-Rabbit (ThermoFisher, A-11008), Alexa Fluor 488 Goat anti-Guinea pig (ThermoFisher, A11073), Alexa Fluor 488 Goat anti-Chicken (ThermoFisher, A-11039), Alexa Fluor 555 Goat anti-Rabbit (ThermoFisher, A21428), Alexa Fluor 555 Goat anti-Rat (ThermoFisher, A21434), Alexa Fluor 555 Goat anti-Guinea pig (ThermoFisher, A21435), Alexa Fluor 647 Donkey anti-Rabbit (ThermoFisher, A31573), Alexa Fluor 647 Goat anti-Chicken (ThermoFisher, A-21449), Alexa Fluor 647 Donkey anti-Guinea pig (Jackson ImmunoResearch, 706-605-148), Alexa Fluor 647 Streptavidin (ThermoFisher, S21374), StarBright Blue 700 anti-Mouse (BioRad, 12004159), StarBright Blue 700 anti-Rabbit

(BioRad, 12004162), CF770 anti-Mouse (Biotium, 20077), CF770 anti-Rabbit (Biotium, 20078) and DAPI solution (Dojindo, 340-07971).

***Primary neuronal culture and HEK293T cell cultures***

Cortical neurons were prepared from E16 mouse embryos with trypsin as described previously[77]. Briefly, following euthanasia, brains were rapidly removed on ice and cortices were dissected. Tissue was digested with trypsin (Wako, 201-16945) and gently triturated with fire-polished glass pipettes. Cells were plated on poly-D-lysine-coated substrates (Corning, 354210) at ~$1.0 \times 10^5$ cells/cm² for imaging cultures and protein preparations, and maintained in Neurobasal Medium (Gibco, 21103049) supplemented with 2% B-27 (17504044) and 1% GlutaMAX (35050061) at 37 °C, 5% $CO_2$.

HEK293T cells (ATCC CRL-11268) were cultured in DMEM (Wako, 044-29765) supplemented with 10% FBS (SeraFrance, SF1400), 100 U/mL penicillin–streptomycin (Wako, 168-23191), 1% GlutaMAX and 1% sodium pyruvate (Wako, 190-14881) at 37 °C in 5% $CO_2$ and passaged approximately every 3 days.

***AAV production***

AAVs were produced as previously described[31]. Briefly, HEK293T cells were plated on six 15-cm culture dishes and transfected with 30 μg of pAd-DELTA F6, 15 μg of serotype plasmid AAV PHP.eB or AAV 2/1 and 15 μg of AAV plasmid with 7.5 mM PEI max (Polysciences, 24765) and OPTI-MEM (Gibco, 31985-070). After 72 h, the cells were lysed in 15 mM NaCl, 5 mM Tris-HCl, pH 8.5, and incubated with 50 U/mL Benzonase (Novagen, Cat#70664) for 30 min at 37 °C. The cell extracts including AAVs, which were obtained by centrifugation at 2,800 × *g* for 30 min at 4 °C, were centrifuged on a gradient of 15%, 25%, 40% and 60% iodixanol solution using a Beckman Ti-70 rotor at 67,000 rpm for 1 h. Virus particles were recovered from the boundary between 40% and 60% iodixanol and concentrated with a 100-kDa filter (Vivaspin, NIPPON Genetics). Virus titres were measured by qPCR using a linearised genome plasmid as a standard (~$2 \times 10^{13}$ genome copies/mL). For small-scale AAV production, $5 \times 10^5$ HEK293T cells were plated on a 12-well dish and cultured in DMEM containing 10% FBS, 1% penicillin–streptomycin, 1% GlutaMAX and 1% sodium pyruvate. The next day, two hours prior to transfection, culture medium was replaced with only 1 mL DMEM, and cells were transfected with 0.8 μg of pAd-DELTA F6, 0.4 μg of serotype plasmid AAV PHP.eB or AAV 2/1 and 0.4 μg of AAV plasmid. After 72 h, the cells were incubated

with 50 U/mL Benzonase for 30 min at 37 °C, after which the AAV-containing supernatant was collected and filtered through a 0.45-μm cellulose acetate Spin-X centrifuge tube filter (Costar, 8162).

***Stereotaxic surgery and viral injections***

Stereotaxic surgeries were performed as previously described with minor modifications[33]. Briefly, mice were deeply anaesthetised via an intraperitoneal injection of 0.1 M phosphate-buffered saline (PBS) containing a three-agent anaesthetic mixture of medetomidine (0.75 mg/kg), midazolam (4 mg/kg) and butorphanol (5 mg/kg) at standard concentrations. Once anaesthetised, each mouse was secured in a stereotaxic frame (RWD, 68803), and ophthalmic ointment was applied to protect the eyes. After removing scalp hair and disinfecting the skin with Betadine, a midline scalp incision was made to expose the skull. Craniotomies were then performed using a microdrill at the designated coordinates for viral injections. Unless otherwise stated, all mPFC injections were made at the following stereotaxic coordinates relative to bregma: anteroposterior (AP), +2.58 mm; mediolateral (ML), ±0.5 mm; dorsoventral (DV), −0.9 mm. For experiments requiring BLA injections, viruses were injected into the BLA at the following coordinates relative to bregma: AP, −1.4 mm; ML, ±3.35 mm; DV, −4.4 mm. Viral injections were performed using a glass capillary (World Precision Instruments, 504950) connected to a Nanoliter 2020 injector (World Precision Instruments). Vectors were delivered at a rate of 85 nL/min, and the needle was left in place for an additional 1 min to allow diffusion before withdrawal. Following injection, the scalp was closed using surgical sutures and tissue adhesive. Mice were placed in a recovery cage under a heat lamp until they regained consciousness and were allowed at least two weeks to recover before further procedures or behavioural testing.

For ActProX-ID experiments, TRAP2 mice were bilaterally injected with 800 nL per hemisphere of AAV-PHP.eB-CaMKII-DIO-ActProX-ID into the mPFC. For ProX-ID experiments, C57BL/6J mice were bilaterally injected with 800 nL per hemisphere of AAV-PHP.eB-CaMKII-ProX-ID into the mPFC. For TSPAN7–TurboID experiments, C57BL/6J mice were bilaterally injected with 800 nL per hemisphere of AAV-PHP.eB-CaMKII-TSPAN7–TurboID into the mPFC. For non-expressing controls, animals received saline injections instead of AAV at the corresponding stereotaxic coordinates and were subjected to the same biotin administration schedule as the corresponding ActProX-ID, ProX-ID or TSPAN7–TurboID groups. For labelling mPFC–BLA projection neurons, TRAP2 or

C57BL/6J mice were bilaterally injected with 800 nL per hemisphere of AAV-CaMKII-DIO-Axon-mCherry or AAV-CaMKII-Axon-mCherry into the mPFC. For labelling anatomically defined mPFC–BLA synapses and behaviourally activated synapses using dual-eGRASP, C57BL/6J mice received bilateral viral injections into the mPFC as the presynaptic region and the BLA as the postsynaptic region. For presynaptic labelling, a total volume of 900 nL per hemisphere of a viral mixture comprising AAV-PHP.eB-CaMKII-Cre, AAV-PHP.eB-FAH-rtTA3, AAV-PHP.eB-EWB-DIO-cyan pre-eGRASP (p32) and AAV-PHP.eB-TIWB-yellow pre-eGRASP (p30) was injected into the mPFC. For postsynaptic complementation, a total volume of 900 nL per hemisphere of a viral mixture comprising AAV-PHP.eB-CaMKII-Cre, AAV-PHP.eB-FAH-rtTA3, AAV-PHP.eB-TIWB-myrmScarlet-I-P2A-post-eGRASP and AAV-PHP.eB-EWB-DIO-myriRFP670V5-P2A-post-eGRASP was injected into the BLA. For gene knock-in experiments using the HiUGE system, TRAP2 mice were bilaterally injected into the mPFC with a total volume of 800 nL per hemisphere containing AAV-PHP.eB-pMecp2-SpCas9-spA and AAV-PHP.eB-HiUGE-TSPAN7-KI. For projection-resolved genetic manipulation experiments, SpCas9 knock-in mice or C57BL/6J mice co-injected with AAV-PHP.eB-pMecp2-SpCas9-spA received bilateral viral injections into the mPFC. For control, TSPAN7-cKO and CPLX2-cKO experiments, a total volume of 800 nL per hemisphere of AAV-PHP.eB-U6-sgRNA(Scramble)_hSyn-mCherry-KASH-bGH, AAV-PHP.eB-U6-sgRNA(Tspan7)_hSyn-mCherry-KASH-bGH or AAV-PHP.eB-U6-sgRNA(Cplx2)_hSyn-mCherry-KASH-bGH was injected into the mPFC. To generate mice expressing the disease-linked TSPAN7 P172H variant in mPFC neurons, AAV-PHP.eB-U6-sgRNA(Tspan7)_hSyn-mCherry-KASH-bGH was co-injected with an sgRNA-resistant AAV-PHP.eB-CaMKII-hTSPAN7(P172H) construct, thereby disrupting endogenous TSPAN7 while expressing the human TSPAN7 P172H variant in mPFC neurons. These mice are referred to as TSPAN7 P172H mice throughout the manuscript.

For electrophysiological experiments, SpCas9 mice were bilaterally injected, into the mPFC, with a total volume of 800 nL per hemisphere of viral mixture containing AAV-PHP.eB-CaMKII-Cre and AAV-PHP.eB-EF1a-DIO-hChR2(H134R)-P2A-EYFP to enable optogenetic activation of mPFC–BLA projections. Control mice received AAV-PHP.eB-U6-sgRNA(Scramble)_hSyn-mCherry-KASH-bGH. TSPAN7-cKO mice received AAV-PHP.eB-U6-sgRNA(Tspan7)_hSyn-mCherry-KASH-bGH. TSPAN7 P172H mice received AAV-PHP.eB-U6-sgRNA(Tspan7)_hSyn-mCherry-KASH-bGH together with AAV-PHP.eB-CaMKII-hTSPAN7(P172H), thereby disrupting endogenous TSPAN7 while expressing the disease-linked human TSPAN7 P172H variant in mPFC neurons.

Mice were group-housed (2–5 per cage) under a 12-h light/dark cycle with *ad libitum* access to food and water. Animals were excluded from analysis if *post hoc* histology revealed off-target injections, unilateral expression or insufficient expression in the target region; exclusion criteria were pre-specified. Final sample sizes are reported in the figure legends and in Supplementary Table 10.

***Immunostaining and imaging analysis***

Immunocytochemistry in cultured neurons was performed as described previously[31,77]. Cultured neurons were transduced with small-scale AAVs at DIV 0 as previously described and fixed at DIV 11 or 14 in 4% paraformaldehyde (PFA) for 20 min at room temperature. For depolarisation experiments, DIV14 neurons were exposed to pre-warmed Tyrode's solution containing 20 mM KCl for 15 min at 37 °C immediately before fixation, whereas control cultures were exposed to Tyrode's solution containing 5 mM KCl. Cells were permeabilised in PBS containing 0.1% Triton X-100 and 5% normal goat serum (NGS) for 30 min at room temperature, incubated with primary antibodies diluted in PBS with 5% NGS overnight at 4 °C, and then incubated with fluorophore-conjugated secondary antibodies diluted in PBS containing 0.01% Triton X-100 and 5% NGS for 2 h at room temperature. Nuclei were counterstained with DAPI, and coverslips were mounted on glass slides using ProLong Diamond Antifade Mountant (Invitrogen, P36961). Immunohistochemistry on brain sections was performed as described previously. Brains were fixed in 4% PFA, coronally or sagittally sectioned with a microslicer (D.S.K.) at a thickness of 50 or 100 μm, and free-floating sections were incubated with primary antibodies diluted in PBS containing 0.1% Triton X-100 and 5% NGS overnight at 4 °C. Sections were then incubated with fluorophore-conjugated secondary antibodies diluted in PBS containing 0.1% Triton X-100 and 5% NGS for 2 h at room temperature. Nuclei were visualised by DAPI staining, and sections were mounted onto glass slides and coverslipped with ProLong Diamond Antifade Mountant (Invitrogen, P36961).

The following primary antibodies were used for immunocytochemistry in cultured neurons (ICC; dilutions in parentheses): rabbit anti-HA (1:1,000), rabbit anti-Homer1 (1:1,000), guinea pig anti-VGLUT1 (1:1,000), mouse anti-α-tubulin (1:2,000), rabbit anti-TSPAN7 (1:1,000), rat anti-HA (1:1,000), rabbit anti-CPLX2 (1:1,000), rabbit anti-SNAP25 (1:1,000), mouse anti-synaptotagmin1 (luminal domain, 1:250) and rabbit anti-mCherry (1:1,000). For brain sections, primary antibodies used for immunostaining included rabbit anti-TSPAN7 (1:500), rabbit anti-Homer1 (1:1,000), guinea pig anti-VGLUT1 (1:2,000), mouse anti-V5 tag

(1:500), mouse anti-Myc (1:500) and rabbit anti-mCherry (1:500). Fluorophore-conjugated secondary antibodies used for both ICC and immunohistochemistry (IHC) were as follows (dilutions in parentheses): Alexa Fluor 488 goat anti-mouse IgG (1:500), Alexa Fluor 488 goat anti-rabbit (1:500), Alexa Fluor 488 goat anti-guinea pig (1:500), Alexa Fluor 488 goat anti-chicken (1:500), Alexa Fluor 555 goat anti-rabbit (1:500), Alexa Fluor 555 goat anti-guinea pig (1:500), Alexa Fluor 647 donkey anti-rabbit (1:500), Alexa Fluor 647 goat anti-chicken (1:500) and Alexa Fluor 647 donkey anti-guinea pig (1:500).

Fluorescence images were acquired on a Zeiss Imager microscope equipped with an Apotome 3 module, or on Zeiss LSM 900 and LSM 980 confocal microscopes using ZEN software, or on stimulated emission depletion (STED) super-resolution microscopes (TCS SP8 STED and STELLARIS STED, Leica Microsystems) using Leica Application Suite software. The individual acquiring images was always blinded to the experimental conditions. Images were quantified and post-processed using FIJI (ImageJ).

For synaptic analysis, 5-µm-thick Z-stacks consisting of 15 optical sections were acquired at high magnification using a Zeiss LSM 900 confocal microscope (63× objective plus 2.5× optical zoom, ZEN software). Each Z-stack was converted into maximum projection images by condensing three consecutive optical sections using FIJI. Colocalisation of VGLUT1 and Homer1 signals was determined using the Image Calculator function in FIJI, and the number of colocalised synaptic puncta was quantified using the Analyze Particles tool or Synbot[78]. For each image, synaptic puncta were quantified within regions of interest (ROIs) of 100 µm² that were carefully selected from areas lacking neuronal cell bodies to minimise background. All image analyses were performed by an investigator blinded to the experimental conditions, and all statistical results are summarised in Supplementary Table 10.

For analysis of dual-eGRASP images, animals were included only when the presynaptic and postsynaptic reporter components were expressed bilaterally in the intended mPFC and BLA regions, respectively, and when off-target or unilateral expression was not detected. Confocal image processing and three-dimensional reconstruction of mPFC–BLA synapses were carried out using ZEN software. All image sets were blinded before evaluation, and identical detection thresholds were applied across all groups. Cyan (CFP) and yellow (YFP) eGRASP signals were automatically detected using ZEN and FIJI and treated as colour-defined synaptic classes generated by independent eGRASP reporter pairs, as previously described for dual-eGRASP analyses[3]. CFP-positive signals were used to define anatomically assigned mPFC–BLA synaptic contacts, whereas YFP-positive signals were used to identify putatively behaviourally reactivated contacts within postsynaptic reporter-positive dendritic regions.

CFP+YFP+ signals were classified as reactivated mPFC–BLA synapses with detectable CFP co-labelling. YFP-positive signals lacking detectable CFP were retained as putatively behaviourally reactivated contacts only when they were located within postsynaptic reporter-positive dendritic regions and within the mPFC–BLA terminal field. The identity of postsynaptic neurons was determined based on membrane-localised fluorescent reporter proteins. Dendrites lacking the relevant CFP or YFP eGRASP signals were excluded from the corresponding pathway-assignment analyses. Synaptic puncta density was quantified within defined ROIs, typically 100 μm², selected from regions devoid of neuronal cell bodies. All image analyses were performed by an investigator blinded to the experimental conditions, and all statistical results are summarised in Supplementary Table 10.

***Synaptotagmin 1 antibody uptake assay***

Synaptotagmin 1 antibody uptake assays were performed in cultured neurons. Neurons were grown on poly-D-lysine-coated glass coverslips in 24-well plates as described above. For live labelling, neurons were washed once with pre-warmed standard Tyrode's solution (129 mM NaCl, 5 mM KCl, 1 mM $MgCl_2$, 2 mM $CaCl_2$, 30 mM glucose and 20 mM HEPES, pH 7.4). Depolarisation-evoked uptake was induced using high-$K^+$ Tyrode's solution containing 20 mM KCl. An antibody against the luminal domain of synaptotagmin 1 was diluted 1:250 in pre-warmed high-$K^+$ Tyrode's solution immediately before use. The antibody-containing solution (300 μL) was added to each well, and neurons were incubated for 30 min at 37 °C in a 5% $CO_2$ incubator to allow antibody uptake during synaptic vesicle exo–endocytosis. After incubation, cells were washed three times with pre-warmed culture medium to remove unbound antibody and then fixed with 4% PFA for 20 min at 4 °C. Coverslips were washed with PBS and processed for permeabilisation, blocking and immunostaining as described in the "Immunostaining and imaging analysis" section. Internalised synaptotagmin 1 antibody was used as a readout of activity-dependent synaptic vesicle recycling at presynaptic boutons.

***Immunoprecipitation***

Tissue or cell pellets were resuspended in HEPES buffer (20 mM HEPES, pH 7.5, 150 mM NaCl, 1 mM EDTA, 1 mM DTT, 0.2% NP-40) supplemented with protease and phosphatase inhibitor cocktails (cOmplete Mini, EDTA-free; PhosSTOP, Roche) and incubated for 1 h at 4 °C with gentle rotation. Lysates were sonicated on ice (3 × 10 s) and clarified by centrifugation at 20,400 × *g* for 10 min at 4 °C. Supernatants were transferred to low protein-binding tubes and precleared with Sepharose beads for 30 min at 4 °C with rotation. After

centrifugation at 1,500 × *g* for 1 min, the supernatant was incubated overnight at 4 °C with mouse anti-V5 antibody. The following day, protein G–Sepharose beads were added, and samples were rotated for 1 h at 4 °C. Beads were collected by centrifugation at 1,500 × *g* for 1 min, and the supernatant was removed. Beads were washed five times with ice-cold wash buffer of the same composition as the lysis buffer. After the final wash, residual buffer was carefully removed, and bound proteins were eluted in Laemmli SDS sample buffer by heating at 95 °C for 5 min before SDS–PAGE and immunoblotting.

***SNARE complex analysis***

Cultured neurons were washed with ice-cold PBS and lysed in buffer containing 50 mM Tris–HCl (pH 7.4), 150 mM NaCl, 1% NP-40, 0.5% Triton X-100 and protease inhibitors. Lysates were cleared by centrifugation at 12,000 × *g* for 10 min at 4 °C. Supernatants were mixed with 4× SDS sample buffer and divided into two equal fractions. One fraction was incubated at 37 °C for 30 min without boiling to preserve SDS-resistant SNARE complexes, whereas the other fraction was heated at 95 °C for 5–10 min to fully dissociate complexes. Both fractions were separated by SDS–PAGE and analysed by immunoblotting using an antibody against SNAP25. Neuronal SDS-resistant SNARE complexes were defined as high-molecular-mass bands (>40 kDa) that were detected in non-boiled samples but absent from the corresponding boiled samples.

***Synaptosome fractionation***

Synaptosome-enriched fractions were prepared from microdissected basolateral amygdala (BLA) using a sucrose step-gradient protocol. All procedures were carried out on ice or at 4 °C. BLA tissue was rapidly dissected in ice-cold PBS and transferred to 1 mL of homogenisation buffer (0.32 M sucrose, 10 mM HEPES–NaOH, pH 7.4, 1 mM EDTA and protease and phosphatase inhibitors). Tissue was homogenised, and a 50-µL aliquot was saved as crude homogenate. The homogenate was centrifuged at 1,000 × *g* for 10 min at 4 °C, and the supernatant was collected into a new tube. The pellet (P1; containing nuclei and tissue debris) was resuspended in 1 mL homogenisation buffer, homogenised again (20 strokes) and centrifuged at 1,000 × *g* for 10 min; the two supernatants were combined to yield the S1 fraction, which contains membranes and synaptosomes. S1 was centrifuged at 30,000 × *g* in a TLA55 rotor for 30 min at 4 °C to obtain the P2 pellet. The P2 pellet was gently resuspended in 500 µL of 0.32 M sucrose and 1 mM $NaHCO_3$ (pH 8.3), and homogenised; a 100-µL aliquot was retained as the total P2 fraction. For sucrose density-gradient separation, 400 µL of the P2

suspension was layered onto a discontinuous gradient consisting of 600 µL each of 0.85 M, 1.0 M and 1.2 M sucrose in 1 mM $NaHCO_3$ (TLS55 tubes) and centrifuged at 120,000 × *g* for 2 h at 4 °C. Three fractions were collected: the interface between 0.32 M and 1.0 M sucrose (myelin-enriched), the interface between 1.0 M and 1.2 M sucrose (synaptosome fraction) and the pellet (mitochondria-enriched). The synaptosome fraction was diluted threefold with 30 mM Tris–HCl, pH 8.0, and centrifuged at 136,000 × *g* in a TLA55 rotor for 30 min at 4 °C. The resulting pellet was resuspended in 0.4 mL of 20 mM Tris–HCl, pH 8.0, and used immediately for downstream biochemical analyses or stored at −80 °C until use.

***SDS–PAGE and immunoblotting***

SDS–PAGE and immunoblotting were performed as previously described[31,77,79]. Protein samples from whole lysates, immunoprecipitates or subcellular fractions were mixed with 2× or 4× Laemmli SDS sample buffer and heated at 95 °C for 5 min or 65 °C for 15 min. Proteins were separated by SDS–PAGE using Mini-PROTEAN electrophoresis systems (Bio-Rad) and transferred onto nitrocellulose membranes (Cytiva, 10600002) using a PowerPac HC power supply (Bio-Rad). Membranes were blocked for 1 h at room temperature in Tris-buffered saline containing 0.1% Tween-20 (TBS-T) and 5% skim milk, and then incubated overnight at 4 °C with primary antibodies diluted in TBS-T. After washing in TBS-T, membranes were incubated for 1 h at room temperature with fluorophore-conjugated secondary antibodies diluted in TBS-T. Signals were detected using a ChemiDoc Touch MP imaging system (Bio-Rad) and quantified with Image Lab software (Bio-Rad) or FIJI. Band intensities were normalised to loading controls, and details of the quantification procedures are provided in the "Statistical analysis" section.

***Differential auditory fear conditioning and TRAP2-based BioID labelling***

Differential auditory fear conditioning in TRAP2 mice was adapted from previous protocols using the Fos2A-iCreER (TRAP2) system for activity-dependent tagging of engram ensembles[5]. TRAP2 (Fos2A-iCreER) mice received bilateral injections of AAV-PHP.eB-CaMKII-DIO-ActProX-ID into the prelimbic (PrL) region of the mPFC and were allowed to recover for at least three weeks before behavioural testing. All procedures were performed in the same sound-attenuated conditioning chambers and using the same shock generator as described above for the fear conditioning test. For differential auditory fear conditioning (day 0), mice were placed in a square chamber (18 × 18 × 30 cm) with a grid floor connected to a

shock generator and enclosed in a sound-attenuating box. Two auditory cues were used: a 4-kHz pure tone (CS+, 30 s, ~75 dB) and a white-noise stimulus (CS–, 30 s, ~75 dB). Following a 3-min baseline period, mice received six baseline tone presentations (3 × CS+ and 3 × CS–, interleaved without shock) and were then presented with three CS+–US pairings and three non-reinforced CS– trials in an interleaved order in the same context. CS+ presentations co-terminated with a 2-s footshock (0.7 mA; unconditioned stimulus, US), whereas CS– trials were never reinforced. Inter-trial intervals were 60–120 s. Mice were removed from the chamber 120 s after the last trial. Freezing behaviour during the last pre-shock period and during CS+ presentations was recorded and quantified using the SMART tracking system as described above. Recent (FR-S) and remote (FR-L) recall sessions were conducted 1 day or 14 days after conditioning, respectively. For recall, mice were returned to the original conditioning context and exposed to a series of CS+ and CS– tones without shock (total session length 8–10 min). Freezing during CS+ presentations was used as a measure of cued fear memory retrieval. No-fear (NF) control mice were exposed to the same sequence of CS+ and CS– tones in the conditioning context without prior pairing with shocks, and home-cage (HC) control mice remained in their home cages. Behavioural performance during recall was analysed in the same way as for the fear conditioning test. To achieve activity-dependent genetic access to recall-activated mPFC neurons and their BLA-projecting terminals, TRAP2 mice received intraperitoneal injections of 4-hydroxytamoxifen (4-OHT) before the recall sessions. 4-OHT (Sigma) was prepared as a 10 mg/mL stock in corn oil. Mice received an intraperitoneal injection of 4-OHT (50 mg/kg body weight) 1 h before tone-cued recall in the conditioning context on day 1 (FR-S) or day 14 (FR-L) after fear conditioning. This timing allowed CreERT2 activation in neurons expressing Fos during the recall-associated tagging window, thereby inducing ActProX-ID expression in recall-activated mPFC neurons. HC and NF control cohorts received the same 4-OHT injection schedule but were either kept in the home cage or exposed to non-reinforced CS+ tones without prior fear conditioning, respectively. Twenty-four hours after the recall session, mice were injected subcutaneously with biotin at 24 mg/kg. BLA tissues were collected 6 h after biotin injection for biochemical enrichment and proteomic analysis. This experimental design separated recall-dependent TRAP2-mediated genetic tagging from the subsequent TurboID-mediated biotinylation period, enabling proteomic profiling of BLA-projecting terminals from mPFC neurons that had been activated during the preceding recall episode.

*Validation of ActProX-ID localisation and synaptosome enrichment*

To assess the subcellular distribution and presynaptic enrichment of ActProX-ID-labelled proteins, BLA tissues were collected from TRAP2 mice after FR-S or FR-L recall and subjected to biochemical fractionation and immunohistochemical analysis. For biochemical analysis, BLA tissues were fractionated into crude homogenate, P2, S2 and synaptosome-enriched fractions as described in the "Synaptosome fractionation" section. Equal amounts of protein from each fraction were separated by SDS–PAGE and analysed by immunoblotting with fluorescent streptavidin, together with antibodies against ActProX-ID-HA and the synaptic markers VGLUT1 and Homer1. Streptavidin signal intensity was quantified across fractions to assess the enrichment of biotinylated proteins in synaptosome-enriched fractions. For imaging-based analysis, brain sections containing the BLA were immunostained with fluorescent streptavidin and antibodies against VGLUT1 and Homer1. Confocal or STED images were acquired from BLA regions containing ActProX-ID-labelled mPFC–BLA terminal fields. ActProX-ID- or streptavidin-positive puncta were classified as synaptically associated when they overlapped with VGLUT1-positive presynaptic boutons. Colocalisation between ActProX-ID-labelled or streptavidin-positive puncta and VGLUT1-positive boutons was quantified using identical thresholds across experimental groups. All image analyses were performed by an investigator blinded to the experimental conditions, and all statistical results are summarised in Supplementary Table 10.

**In vivo *BioID protein purification***

*In vivo* BioID experiments were performed as previously described with some modifications[28,31]. For ActProX-ID samples, AAV-PHP.eB-CaMKII-DIO-ActProX-ID was injected into the mPFC of 6-week-old TRAP2 mice. Three weeks after virus injection, mice received biotin as described above, and BLA tissues were dissected 6 h after biotin administration. For ProX-ID samples, AAV-PHP.eB-CaMKII-ProX-ID was injected into the mPFC of 6-week-old mice. Three weeks after virus injection, biotin (24 mg/kg, s.c.) was administered, and BLA tissues were dissected 6 h later. For non-expressing controls, animals received saline injections instead of AAV at the corresponding stereotaxic coordinates and were subjected to the same biotin administration schedule as the corresponding ActProX-ID, ProX-ID or TSPAN7–TurboID groups. Biological replicates per group were as follows: ActProX-ID (HC, NF, FR-S, FR-L; $n$ = 3 each), ProX-ID ($n$ = 3), non-expressing control for ProX-ID ($n$ = 3), TSPAN7–TurboID ($n$ = 3), non-expressing control for TSPAN7–TurboID ($n$ = 4). For each *in vivo* BioID experiment, BLA tissue from a single mouse was used for each biotinylated protein purification, and each purification was performed independently at least

three times. BLA tissues were dissected and lysed in a buffer containing 50 mM Tris-HCl (pH 7.5), 150 mM NaCl, 1 mM EDTA and a protease inhibitor mixture (cOmplete Mini EDTA-free, Roche). An equal volume of detergent-containing lysis buffer was then added to yield final concentrations of 50 mM Tris-HCl (pH 7.5), 150 mM NaCl, 1 mM EDTA, 0.2% SDS, 1% Triton X-100, 1% deoxycholate, protease inhibitor mixture and phosphatase inhibitor mixture. Samples were sonicated and centrifuged at 15,000 × *g* for 10 min. The supernatant was further ultracentrifuged at 100,000 × *g* for 30 min at 4 °C. SDS was added to the cleared supernatant to a final concentration of 1%, and samples were heated at 65 °C for 15 min. After cooling on ice, samples were incubated with Pierce High Capacity NeutrAvidin Agarose beads (Thermo Fisher Scientific) at 4 °C overnight. The beads were washed twice with 2% SDS, twice with 1% Triton X-100, 1% deoxycholate and 25 mM LiCl, twice with 1 M NaCl and five times with 50 mM ammonium bicarbonate. Biotinylated proteins were eluted in a buffer containing 125 mM Tris-HCl (pH 6.8), 4% SDS, 0.2% β-mercaptoethanol, 20% glycerol and 3 mM biotin at 65 °C for 15 min.

***Affinity purification of biotinylated proteins followed by mass spectrometry***

For each *in vivo* BioID experiment, BLA tissue from a single mouse was used for each biotinylated protein purification. Each BLA sample was lysed in 0.5 mL of guanidine-TCEP buffer (7 M guanidine-HCl, 100 mM HEPES-NaOH, pH 7.5, 10 mM TCEP and 40 mM chloroacetamide). The lysates were heated, sonicated and centrifuged at 20,000 × *g* for 15 min at 4 °C. Supernatants were collected, and proteins (2 mg per sample) were purified by methanol–chloroform precipitation and solubilised in 150 µL of a buffer containing 8 M urea, 1% SDS, 50 mM Tris-HCl (pH 7.5) and 150 mM NaCl. After sonication, the protein solutions were diluted eightfold with a buffer containing 50 mM Tris-HCl (pH 7.5) and 150 mM NaCl. Biotinylated proteins were captured by incubation with a 10-µL slurry of NanoLink streptavidin magnetic beads (Vector) for 3 h at 4 °C. The beads were washed three times with a buffer containing 1 M urea, 0.125% SDS, 50 mM Tris-HCl (pH 7.5) and 150 mM NaCl, followed by three washes with 1 M urea and 50 mM ammonium bicarbonate. Proteins on the beads were digested with 400 ng of trypsin/Lys-C mix (Promega) overnight at 37 °C. The digested peptides were acidified and desalted using GL-Tip SDB (GL Sciences). The eluates were evaporated in a SpeedVac concentrator and reconstituted in 0.1% trifluoroacetic acid and 3% acetonitrile (ACN).

LC–MS/MS analysis of the resulting peptides was performed by data-independent acquisition (DIA) on a Q Exactive Plus mass spectrometer coupled to an EASY-nLC 1200 UHPLC via a nanoelectrospray ion source (Thermo Fisher Scientific). Peptides were separated on a 75-μm inner diameter × 150 mm C18 reversed-phase column (Nikkyo Technos) with a linear gradient of 4–32% ACN for 0–100 min followed by an increase to 80% ACN for 10 min and a final hold at 80% ACN for 10 min. MS1 spectra were acquired over an *m/z* range of 495–750, with a resolution of 17,500, an AGC target of 3e6 and a maximum injection time of 55 ms. MS2 spectra were acquired with a resolution of 35,000 and an AGC target of 3e6, and the maximum injection time was set to auto. DIA employed an 8-Da isolation window scheme with a 4-Da overlap, generated by Scaffold DIA. DIA-MS data were analysed with DIA-NN (version 1.8.1). Raw data files were converted to .dia format and searched against an *in silico*-predicted spectral library generated from the UniProt mouse protein sequence database. The search space was defined with trypsin as the digestion enzyme, one allowed missed cleavage, peptide lengths of 7–45 amino acids, precursor charges of 2 to 4 and a fragment ion *m/z* range of 200–1,800. MS1 and MS2 mass accuracies were set to auto, and all other parameters were kept at default settings.

***Proteome data analysis***

*Proteome data preprocessing and definition of significantly enriched proteins*. For ActProX-ID, normalised abundance values exported from DIA-NN were further processed using Perseus (version 2.0.1.1). Values were $\log_2$-transformed, and no imputation was applied at this stage. For ProX-ID, TSPAN7-TurboID and the corresponding control samples, normalised abundance values exported from DIA-NN were further processed using Perseus (version 2.0.1.1). Proteins were retained only if they were detected in at least three samples across all experimental groups. Values were $\log_2$-transformed, and missing values were imputed using random numbers drawn from an ideal Gaussian distribution (width = 0.3; downshift = 1.8). Differential protein biotinylation level between control and ActProX-ID / ProX-ID / TSPAN7-TurboID samples was evaluated using two-tailed Student's *t*-tests. In this study, proteins meeting both $P < 0.05$ and a $\log_2$ fold change > 2 versus corresponding controls were defined as significantly enriched. For ActProX-ID, the HC (home cage) and NF (no-fear) groups served as behavioral baseline controls for FR-S (fear memory recall-short) and FR-L (fear memory recall-long) samples. Proteins that met the above criteria in both FR-S vs HC and FR-S vs NF

comparisons were defined as FR-S–enriched proteins; FR-L–enriched proteins were defined analogously.

*Functional annotations for the heatmap.*

Proteins were annotated for the following functional categories shown in the right panel of the heatmap, where black indicates annotated proteins and white indicates non-annotated proteins. The Presynapse category was defined using a manually curated list of canonical presynaptic proteins, including synaptic vesicle proteins, active zone components, release machinery and presynaptic voltage-gated ion channels, assembled from the literature. The PAZ, SNARE, Channel and Memory categories were annotated based on composite sets of Gene Ontology (GO) terms defined in this study; the GO IDs used for each category are listed in Supplementary Table 9. The scRNA-seq category was annotated based on overlap with remote memory-associated differentially expressed genes that were upregulated in fear recall (FR) versus no-fear (NF) conditions in excitatory neuron clusters EXH C0, C1 and C3 reported in Chen et al., 2020 [13].

*Cellular component annotation and over-representation analysis.* GO Cellular Component annotations of the identified proteins were assigned using the MGI (Mouse Genome Informatics) database, with classification based on the following terms: cytoplasm (GO:0005737), plasma membrane (GO:0005886), cytoskeleton (GO:0005856), mitochondrion (GO:0005739), Golgi apparatus (GO:0005794), endoplasmic reticulum (GO:0005783), endosome (GO:0005768), synaptic vesicle (GO:0008021) and presynaptic active zone (GO:0048786). UniProt IDs were first converted to MGI gene IDs using a UniProt-to-MGI conversion table downloaded from the UniProt website. Fisher's exact test was performed for each GO CC term using the full list of UniProt IDs from the ID conversion table as the background reference set. Adjusted *p*-values were calculated using the BH-FDR method.

*STRING subcellular compartment localization scoring*. Subcellular localization confidence scores (range 0–5) were retrieved using the stringApp (v2.2.0)[80] plugin in Cytoscape 3.10.3 [28,31]. For each compartment of interest (indicated in the corresponding figure), scores from the compartment_stringdb:: node attribute columns were averaged across the protein group of interest, without applying any cutoff.

*SynGO analysis*. For SynGO analysis[34], UniProt IDs were converted to MGI gene IDs using the conversion table described above, and subsequently to HGNC IDs using the HGNC Comparison of Orthology Predictions (HCOP) database (https://www.genenames.org/tools/hcop/) for input into SynGO[34] (release 1.3; background: Brain expressed; minimum number of genes per GO term: 3).

*Annotation and over-representation analysis for known presynaptic proteins and neurological disease-associated proteins.* Known presynaptic proteins were defined as those included in the presynaptic gene set retrieved as a list of MGI gene IDs using the getAllGenes4Compartment() function from the synaptome.db package. Neurological disease-associated genes were identified using the getGeneDiseaseByIDs function for DO terms listed in Supplementary Table 8. Human Entrez Gene IDs obtained from synaptome.db were first converted to MGI gene IDs using the HGNC Comparison of Orthology Predictions (HCOP) database (https://www.genenames.org/tools/hcop/). The resulting MGI gene IDs were then converted to UniProt IDs using the UniProt-to-MGI conversion table described above, for subsequent comparison with our proteomic dataset. Fisher's exact test was performed for the known presynaptic proteins and disease-associated proteins using the full list of UniProt IDs from the ID conversion table as the background reference set. Adjusted *p*-values were calculated using the BH-FDR method.

*Annotation of functionally uncharacterised proteins*. Proteins with no GO annotations, or with GO annotations supported only by low-evidence codes (IBA, IBD, IKR, IRD, ISS, ISO, ISA, ISM, IGC, RCA, TAS, NAS, IC, ND, IEA), were classified as functionally uncharacterised proteins (GO).

*Candidate prioritisation.* Candidate proteins for experimental validation were prioritised after statistical identification of recall-enriched ActProX-ID proteins. First, proteins were required to meet the enrichment criteria described above in FR-S and/or FR-L ActProX-ID datasets relative to matched HC and NF controls. Second, candidates were evaluated for recall-phase bias, with priority given to proteins preferentially represented in, or experimentally validated under, the FR-L condition. Third, candidates were cross-referenced with the steady-state mPFC–BLA ProX-ID dataset to determine whether they were detectable within the projection-defined presynaptic proteome. Fourth, proteins were annotated for synaptic, membrane-associated, vesicle-related or release-site-associated features using the GO Cellular Component,

SynGO, SynaptomeDB and KEGG BRITE annotations described above. Finally, neurological or psychiatric disease relevance was assigned using the disease-associated gene annotations described above and curated literature supporting neurological or psychiatric disease relevance. The functionally uncharacterised category was used for dataset-level annotation and was not applied as an absolute exclusion criterion during candidate selection. Proteins were not excluded solely because they had prior functional annotations; instead, priority was given to candidates whose projection-specific, recall-associated or *in vivo* presynaptic roles were poorly characterised.

*Annotation for Biological Process and Molecular Function and over-representation analysis.* Multi-list GO enrichment analysis was performed using Metascape (http://metascape.org) using its multi-gene-list input. For each analysis, the gene sets of projection-identified and/or projection-enriched proteins shown in the corresponding figure panel were submitted to Metascape as multiple gene lists. We specifically employed the Custom Analysis workflow to refine our analysis to select ontology catalogues including Biological Process and Molecular Function. To broadly assess GO annotation, the background was defined as the default species genome (*M. musculus*). The enrichment parameters were set to default thresholds: minimum 3 genes per term, $p \leq 0.01$ and enrichment factor $\geq 1.5$. Dot plots were generated using the output from Metascape (metascape_result.xlsx and HeatmapSelectedGO.csv) and visualised in MATLAB. The plots display the $-\log_{10}$(p-value) and the percentage of annotated proteins relative to the total input for the top 20 enriched terms.

*Visualisation*. Protein–term networks were generated based on annotations from the KEGG BRITE database[81–83]. For visualisation, the KEGG BRITE terms in the following categories were used: BRITE Hierarchy (09180) and Environmental Information Processing (09130) in KEGG Orthology [BR:mmu00001] (https://www.kegg.jp/brite/mmu00001), Membrane Trafficking [BR:mmu04131] (https://www.kegg.jp/brite/mmu04131), Ion Channels [BR:mmu04040] (https://www.kegg.jp/brite/mmu04040), Transporters [BR:mmu02000] (https://www.kegg.jp/brite/mmu02000) and GTP-Binding Proteins [BR:mmu04031] (https://www.kegg.jp/brite/mmu04031). To improve visual clarity, some categories were merged and manually labelled. For proteins associated with multiple terms, a subset of associations was not displayed to maintain the interpretability of the network. Protein–protein interaction (PPI) networks were constructed using the stringApp plugin in Cytoscape[84].

***Marmoset spatial transcriptomics***

Marmoset 10x Visium data were obtained from a previous study[85]. The mPFC was manually delineated based on H&E staining patterns. Analyses were conducted using the *Seurat* R package (v5.3.0)[86]. The data were processed with the following *Seurat* functions: *SCTransform* for normalisation, *RunPCA* for dimensionality reduction, *FindNeighbors* for computation of the nearest neighbours and *FindClusters* for cluster identification. Cortical layer 2 and layer 3 clusters were then defined based on characteristic cortical layer markers in combination with their spatial localisation. After batch correction using the *Harmony* R package[87], the mean expression levels of genes identified in the mPFC-BLA proteome were calculated using the *Seurat* R package. All analyses were performed in R (4.4.1).

***Behavioural analysis***

Control mice, mice with mPFC-targeted *Tspan7* disruption and mice expressing human TSPAN7 P172H on a *Tspan7*-disrupted background were subjected to a behavioural battery in the following order: open field test, elevated plus maze (EPM) test, three-chamber social interaction test and cued and contextual fear conditioning test. The open field, EPM and three-chamber tests were conducted in a sound-attenuated room, where mice were also habituated for 1 h prior to each test. The fear conditioning test was conducted in a conditioning chamber enclosed within a sound-attenuating box, and, prior to testing, mice were habituated for 1 h in a separate sound-attenuated room distinct from the testing chamber. All apparatuses were cleaned between animal trials using slightly acidic electrolyzed water to eliminate olfactory cues, except for the grid floor of the fear conditioning chamber, which was cleaned with 70% ethanol and distilled water. Behavioural testing was performed between 9:00 a.m. and 6:00 p.m., with the order of animals tested counterbalanced across groups. Each behavioural test was conducted on a separate day. Mouse behaviours were recorded using a video camera and analysed by the SMART 3.0 video tracking system (Panlab Harvard Apparatus, Spain).

*Open field test.* The apparatus consisted of a white square cage (50 × 50 × 30 cm; O'Hara) with the floor divided into a 6 × 6 grid of equal squares and illuminated at 40 lux. Each mouse was placed in the bottom-left corner of the arena and allowed to explore freely for 10 min. Behavioural activity was recorded, and the following parameters were quantified: total distance traveled (cm), time spent in the centre area (the 4 × 4 grid inside the overall 6 × 6 grid) (s), time spent immobile (s) and mean velocity without time spent immobile (cm/s).

*EPM test.* The apparatus consisted of two arms (25 × 5 cm) with 3-mm-high ledges along the sides and distal end (open arms) and two closed arms (25 × 5 cm) with transparent walls (15 cm high) enclosing the sides and distal ends (Shin Factory). Arms of the same type were positioned opposite each other and connected by a central square platform (5 × 5 cm), with all surfaces made of grey plastic. The maze was elevated 50 cm above the floor and illuminated at 100 lux at the centre. Each mouse was placed in the central square facing a closed arm and allowed to explore for 10 min. Behavioural activity was recorded, and the following parameters were quantified: total distance traveled (cm), time spent in the open arms (s), number of open-arm entries and ratio of open-arm entries to total arm entries.

*Three-chamber social interaction test.* The apparatus comprised a three-chamber rectangular structure with grey walls and floors and transparent dividing walls (Shin Factory). Each chamber measured 20 × 40 × 22.5 cm and was connected by walls containing small rectangular openings (5.5 × 8.5 cm) to allow free movement between chambers. On the day prior to testing, mice were habituated for 10 min in the central chamber, followed by 10 min of free exploration across all three chambers. On the test day, mice were again placed in the central chamber for 5 min and then allowed to explore all chambers freely for another 5 min. Following this exploration, a novel, age- and sex-matched C57BL/6J mouse (referred to as the stranger mouse) was placed inside a wire cage in one of the side chambers, while an identical but empty wire cage was placed in the opposite chamber. The test mouse was allowed to explore freely for 10 min. Behavioural activity was recorded, and the following parameters were quantified: total distance traveled (cm), time spent in the zone surrounding the cage containing the stranger mouse (social interaction time, s) and time spent in the zone surrounding the empty cage (empty cage time, s). Mouse behaviour was analysed using SMART 3.0 with two tracking points for zone quantification. Time spent in the cage-vicinity zone was computed based on the mouse body centre (centroid), whereas time spent in the sniffing zone was computed based on the nose point (tip of the snout). A social interaction score was calculated as: (social interaction time − empty cage time)/(social interaction time + empty cage time).

*Fear conditioning test.* Each mouse was placed in a chamber (19 × 20 × 25 cm; context A) with a black wall, enclosed in a sound-attenuating box and illuminated at 200 lux. After 4 min of free exploration, the mice were exposed to a 30-s auditory tone (8 kHz, 70 dB; conditioned stimulus, CS) that coterminated with a 2-s foot shock (0.3 mA; unconditioned stimulus, US). This CS–US pairing was repeated three times with 130-s interstimulus intervals. Mice were

removed from the chamber 130 s after the final pairing. Freezing behaviour during the test period was measured to assess fear acquisition.

Contextual and cued memory tests were performed in the same cohort of mice either 1 day or 14 days after conditioning. Contextual memory retrieval was assessed first by returning mice to the original conditioning chamber (context A), where they were observed for 12 min without any stimulus presentation. Freezing behaviour during the 12-min period was measured to assess contextual memory retrieval. After an inter-test interval, cued memory retrieval was assessed in a novel environment (context B; 18 × 18 × 15 cm, white chamber). Mice were placed in context B for a total of 8 min, consisting of a 3-min baseline period without the CS, a 3-min CS presentation (8 kHz, 70 dB) and a 2-min post-CS period. Freezing behaviour during the CS presentation period was measured to assess cued memory retrieval. The conditioning apparatus was controlled using Packwin software (Panlab Harvard Apparatus) on a PC. Freezing, defined as the complete absence of body movement except for respiration lasting at least 2 s, was automatically analysed using the SMART system (Panlab Harvard Apparatus). The recall conditions used for each experimental dataset are summarized in Supplementary Table 1.

***Electrophysiological analysis***

For electrophysiological experiments, SpCas9 mice received bilateral injections of AAVs into the mPFC 2–3 weeks before slice recordings. To enable optogenetic activation of mPFC–BLA projections, mice received AAV-PHP.eB-CaMKII-Cre and AAV-PHP.eB-EF1a-DIO-hChR2(H134R)-P2A-EYFP, together with the indicated sgRNA or rescue viruses. Coronal brain slices containing the BLA were prepared as previously described[88]. In brief, mice were anaesthetised with isoflurane and transcardially perfused with ice-cold modified artificial cerebrospinal fluid (mACSF) containing 222.1 mM sucrose, 27 mM $NaHCO_3$, 1.5 mM $NaH_2PO_4$, 2.5 mM KCl, 0.5 mM ascorbic acid, 1 mM $CaCl_2$ and 7 mM $MgSO_4$. After decapitation, brains were rapidly removed and transferred into ice-cold, oxygenated mACSF. Coronal slices containing the BLA (300 μm thick) were cut using a vibrating microtome (VT1200S; Leica Microsystems, Wetzlar, Germany) at a cutting speed of 100 μm/s. The slices were then transferred to oxygenated artificial cerebrospinal fluid (ACSF) at 35 °C, consisting of 127 mM NaCl, 1.6 mM KCl, 1.24 mM $KH_2PO_4$, 1.3 mM $MgSO_4$, 2.4 mM $CaCl_2$, 26 mM $NaHCO_3$ and 10 mM D-glucose, and incubated for 30 min. Subsequently, the slices were maintained at room temperature for at least 30 min until electrophysiological recordings.

Slices were transferred to a recording chamber, where oxygenated ACSF at 32 °C was continuously perfused at a flow rate of 3–4 mL/min. Whole-cell voltage-clamp recordings were obtained from visually identified BLA principal neurons in regions containing EYFP-positive mPFC–BLA axon terminals. Patch pipettes were filled with an internal solution containing 130 mM $CsMeSO_4$, 10 mM CsCl, 10 mM HEPES, 10 mM phosphocreatine-$Na_2$, 4 mM MgATP, 0.3 mM NaGTP and 5 mM QX-314; pH 7.2–7.3, 280–295 mOsm. The pipette tip resistance was 3–6 MΩ. Synaptic currents were recorded using a computer-controlled amplifier (MultiClamp 700B, Molecular Devices). Data were sampled at 20 kHz, digitised with an analog-to-digital converter (Digidata 1440A, Molecular Devices) and stored on a personal computer using pCLAMP 10.7 acquisition software (Molecular Devices). sEPSCs were recorded in voltage-clamp mode at a holding potential of –70 mV for 5 min. Series resistance was monitored throughout the recording, and cells were excluded from analysis if it exceeded 30 MΩ or varied by more than 25%. All data were analysed using custom-written scripts in MATLAB (MathWorks). For sEPSCs, frequency and amplitude were quantified over a 1-min period.

To record light-evoked EPSCs (leEPSCs), optical stimuli at 465 nm with a duration of 5 ms were applied to the recording area using a light-emitting diode (LED; LEX2, Brain Vision). Pairs of optical pulses were delivered with an inter-stimulus interval of 100 ms. For each trial, the baseline current was calculated over a 2-s window immediately before the first stimulus and subtracted from the trace. Typically, five consecutive trials were averaged to obtain a representative leEPSC waveform for each cell. The paired-pulse ratio (PPR) was calculated as the ratio of the peak amplitude of the second leEPSC to that of the first leEPSC (leEPSC2/leEPSC1).

***Quantification and statistical analysis***

Statistical analyses were performed exclusively on experimental data using GraphPad Prism v9 (GraphPad Software). Data are expressed as the mean ± s.e.m. We compared independent sample means using Student's *t*-tests, one-way ANOVAs and two-way ANOVAs as appropriate. Statistically significant F-values detected in the ANOVAs were followed by alpha-adjusted *post-hoc* tests (Tukey's HSD or Šídák's test). $P < 0.0001$, $P < 0.001$, $P < 0.01$ and $P < 0.05$ were considered to indicate statistical significance. Sample size is indicated in the figure legend for each experiment. Sample sizes were not predetermined by statistical methods but were based on our previous experience and on similar experiments in the literature, which

yielded sufficient power to detect the expected effects. All results of the statistical analysis are shown in Supplementary Table 10.

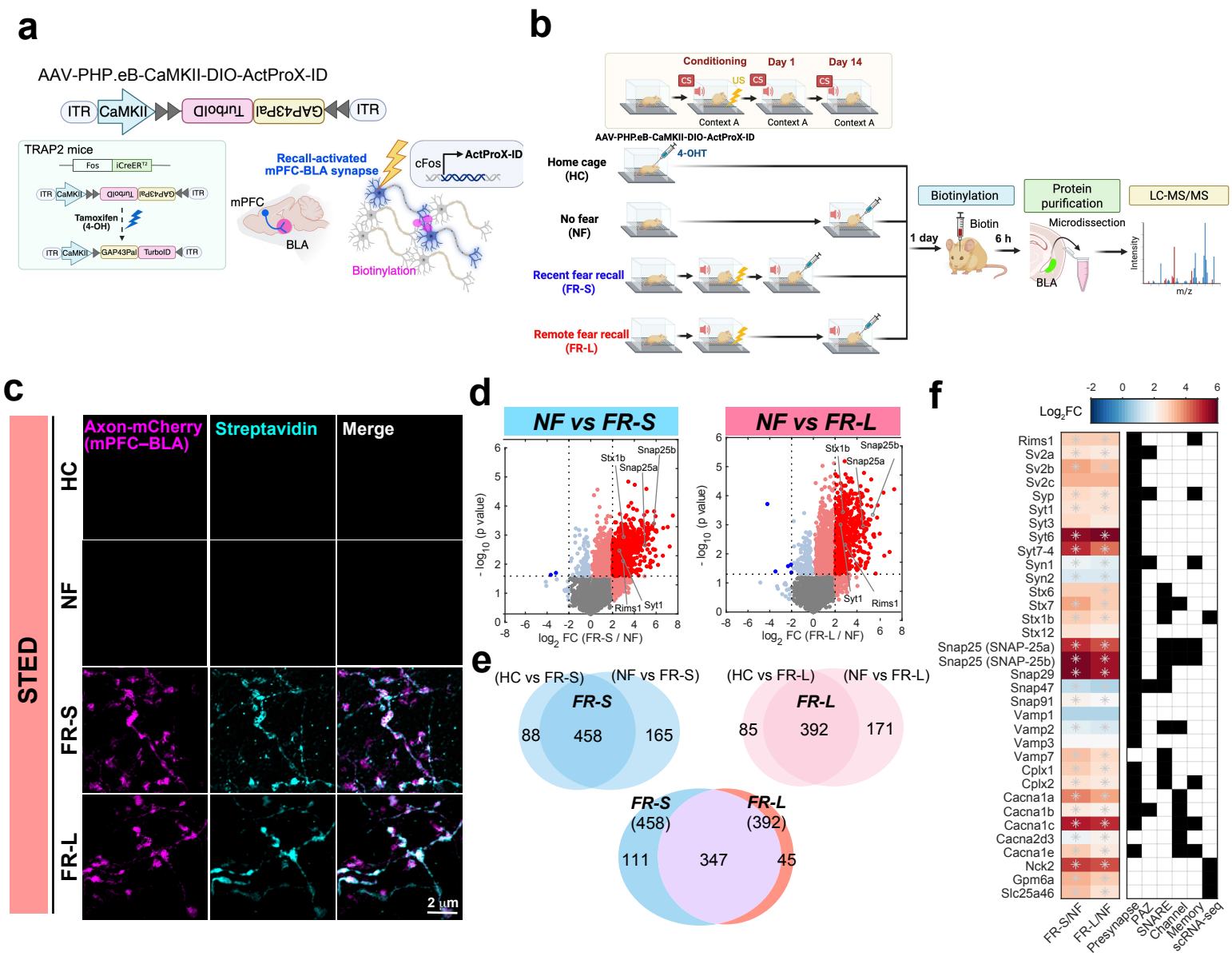


**Figure 1. Development and validation of ActProX-ID for activity-gated, projection-resolved profiling of presynaptically enriched proteomes in the mPFC–BLA pathway. a**, Schematic of the ActProX-ID strategy. In TRAP2 mice, recall-associated neuronal activity induces cFos–CreERT2 in mPFC neurons, and 4-OHT enables Cre-dependent expression of presynaptically targeted TurboID. Systemic biotin administration labels proteins in presynaptically enriched compartments of mPFC–BLA projection neurons genetically captured during fear-memory recall. **b**, Experimental design for *in vivo* ActProX-ID labelling and proteomic analysis. Adult TRAP2 mice received AAV-PHP.eB-CaMKII-DIO-ActProX-ID injections into the prelimbic mPFC and were assigned to home-cage control (HC), no-fear control (NF), recent fear recall (FR-S) or remote fear recall (FR-L) groups. Mice underwent differential auditory fear conditioning on day 0 and recall testing on day 1 or day 14. 4-OHT was administered 1 h before recall, biotin was administered the following day, and BLA tissue was collected 6 h after biotin administration for streptavidin enrichment and LC–MS/MS analysis. **c**, Representative STED images showing streptavidin-labelled ActProX-ID puncta in activity-dependently labelled, axon-mCherry-positive mPFC–BLA projection boutons in HC, NF, FR-S and FR-L mice. **d**, Volcano plots showing $\log_2$ fold change versus $-\log_{10} P$ value for ActProX-ID-labelled proteins in FR-S and FR-L mice compared with NF controls. Dashed lines indicate $P = 0.05$ (horizontal) and $\log_2$ fold change = −2 and 2 (vertical). Red dots indicate significantly enriched proteins with $\log_2$ fold change > 2.0 and $P < 0.05$. **e**, Venn diagrams showing the overlap between FR-S- and FR-L-associated biotinylated proteins identified by ActProX-ID. Top: FR-S-associated (left) and FR-L-associated (right) proteins were defined as those significantly enriched relative to both HC and NF controls ($\log_2$ fold change > 2.0, $P < 0.05$). Bottom: overlap between the FR-S- and FR-L-associated sets. Recall-associated proteins were defined as proteins enriched in FR-S or FR-L mice relative to both HC and NF controls using the criteria of $\log_2$ fold change > 2.0 and $P < 0.05$. Numbers indicate FR-S-associated, FR-L-associated and FR-S/FR-L-common proteins. **f**, Heatmap of normalised $\log_2$ biotinylation levels relative to NF controls for representative presynaptic proteins, memory-related proteins and remote-memory-associated genes. Asterisks indicate proteins significantly enriched in ActProX-ID samples according to the criteria of $\log_2$ fold change > 2.0 and $P < 0.05$. The right panel shows binary annotations for each protein across functional categories (see Methods).

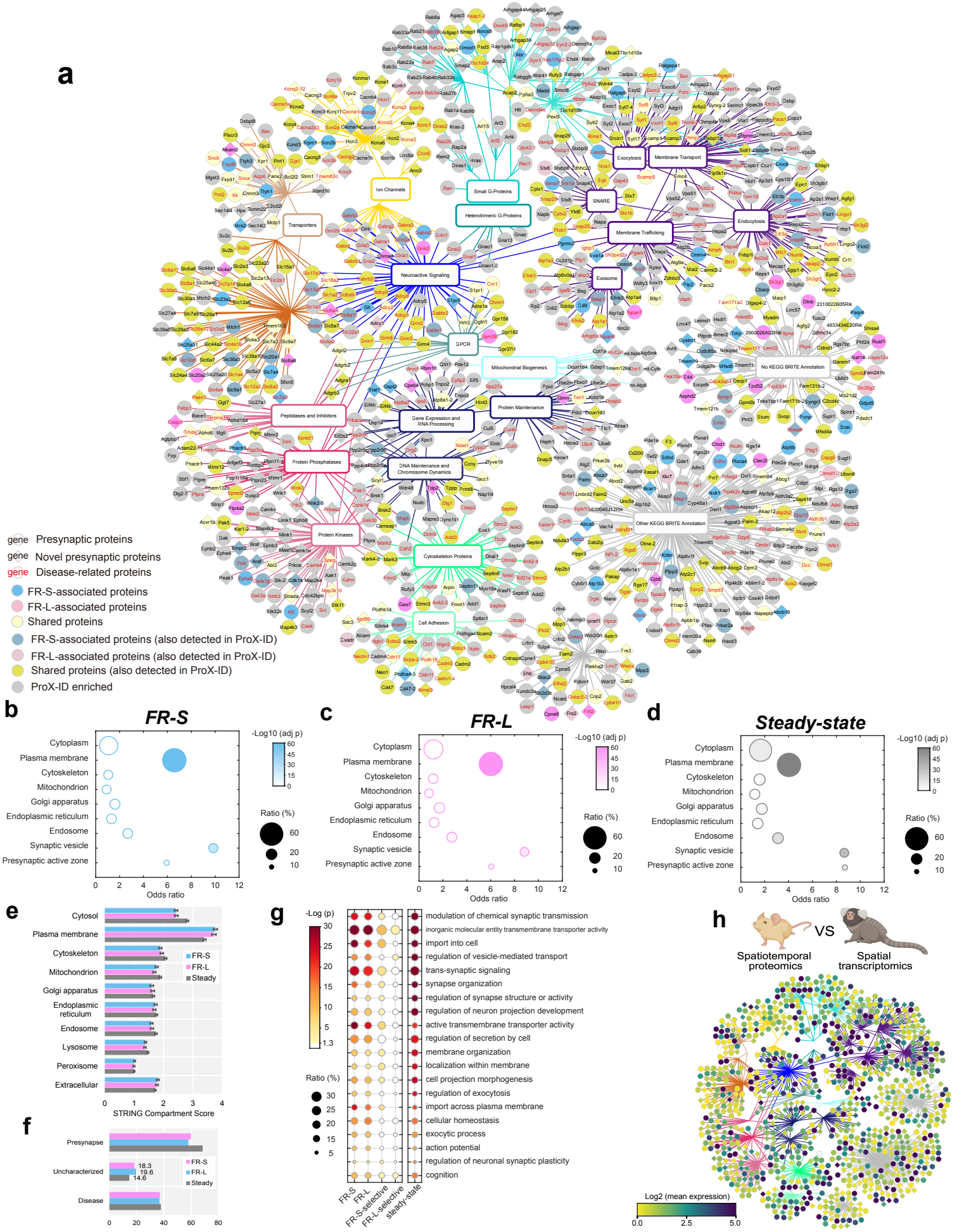


**Figure 2. ActProX-ID reveals recall-associated, phase-biased organisation of presynaptically enriched proteomes in the mPFC–BLA pathway. a**, Protein–term network based on KEGG BRITE annotations. Nodes represent proteins and functional terms, and edges indicate associations based on BRITE functional categories. A numerical suffix in some of the node labels (e.g., '-4' in Ank2-4) corresponds to the UniProt isoform number. **b–d**, Bubble plots summarizing enrichment analysis of selected Gene Ontology (GO) Cellular Component terms for FR-S-associated proteins (**b**), FR-L-associated proteins (**c**) and steady-state ProX-ID proteins (**d**). **e**, Averaged STRING compartment scores for FR-S-associated, FR-L-associated and steady-state ProX-ID proteins. Data are presented as mean ± s.e.m. **f**, Functional classification of recall-associated and steady-state ProX-ID proteins into known presynaptic, neurological disease-associated and functionally uncharacterized categories. **g**, Top enriched GO Biological Process and Molecular Function terms for FR-S-selective, FR-L-selective, FR-S, FR-L and steady-state ProX-ID protein sets. **h**, Gene expression levels in layer 2 of the six-month-old marmoset mPFC, visualised in the protein–term network.

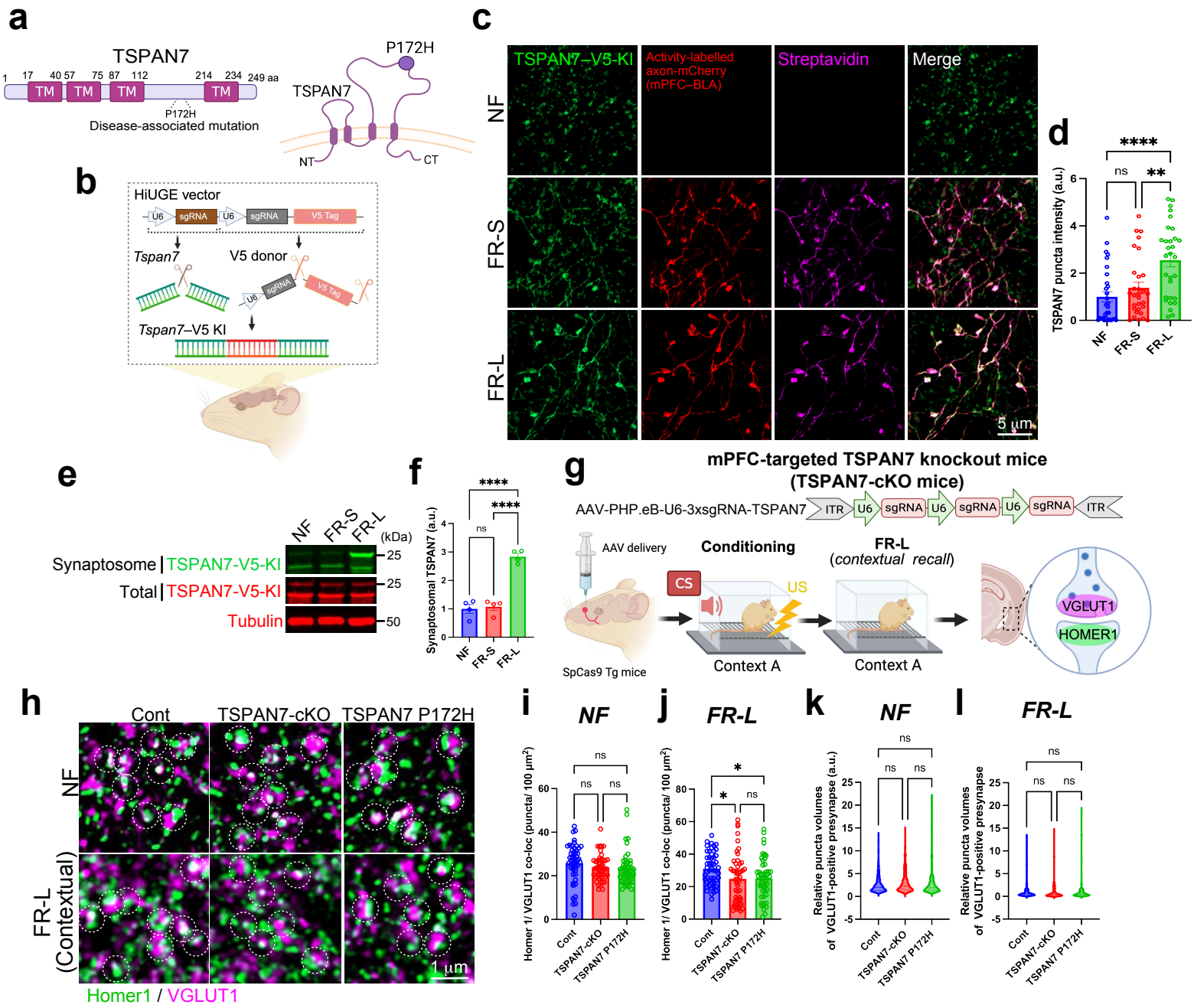


**Figure 3. TSPAN7 accumulates at mPFC–BLA presynaptic terminals during contextual fear-memory recall and is required for recall-associated synaptic remodelling. a**, Schematic domain organization of TSPAN7, a tetraspanin with four predicted transmembrane (TM) domains. The disease-associated P172H substitution in the large extracellular loop is indicated. **b**, Schematic of the homology-independent universal genome engineering (HiUGE) strategy used to generate endogenous TSPAN7–V5 knock-in labelling in mPFC neurons. **c**, Representative confocal images of BLA sections from TSPAN7–V5 knock-in mice expressing ActProX-ID and axon-mCherry in mPFC–BLA projection neurons after no-fear exposure or recent/remote contextual fear-memory recall. Images show TSPAN7–V5 signals together with axon-mCherry-positive mPFC–BLA projections and streptavidin-labelled ActProX-ID puncta. **d**, Quantification of TSPAN7–V5 puncta intensity in axon-mCherry-positive mPFC–BLA projection fields across behavioural conditions. Data are presented as mean ± s.e.m.; $n = 14–15$ slices from four mice per group. One-way ANOVA with Tukey's multiple-comparisons test. $^{****}P < 0.0001$, $^{**}P < 0.01$; ns, not significant. **e**, Immunoblot analysis of TSPAN7–V5 in total lysates and synaptosome-enriched fractions from TSPAN7–V5 knock-in mice subjected to NF, FR-S or FR-L contextual fear-memory recall, with tubulin as a loading control. **f**, Quantification of synaptosomal TSPAN7–V5 levels across behavioural conditions, normalized to total TSPAN7-V5 expression. Data are presented as mean ± s.e.m.; $n = 4$ mice. One-way ANOVA with Tukey's multiple-comparisons test. $^{****}P < 0.0001$; ns, not significant. **g**, Schematic of AAV-based mPFC-targeted deletion of *Tspan7* in SpCas9 transgenic mice. Mice with TSPAN7 disruption in mPFC projection neurons underwent fear conditioning and remote contextual fear recall, followed by immunostaining of BLA sections for Homer1 and VGLUT1. **h**, Representative confocal images of Homer1/VGLUT1-positive excitatory synapses in the BLA of control, TSPAN7-cKO and TSPAN7 P172H mice under NF and remote contextual fear recall conditions (FR-L). **i–l**, Quantification of Homer1/VGLUT1-positive excitatory synapse density (**i**,**j**) and VGLUT1-positive presynaptic puncta volume (**k**,**l**) across genotypes and behavioural conditions. Data are presented as mean ± s.e.m.; $n =$ 36–51 images from 15 slices obtained from four mice per group. One-way ANOVA with Tukey's multiple-comparisons test. $^{*}P < 0.05$; ns, not significant.

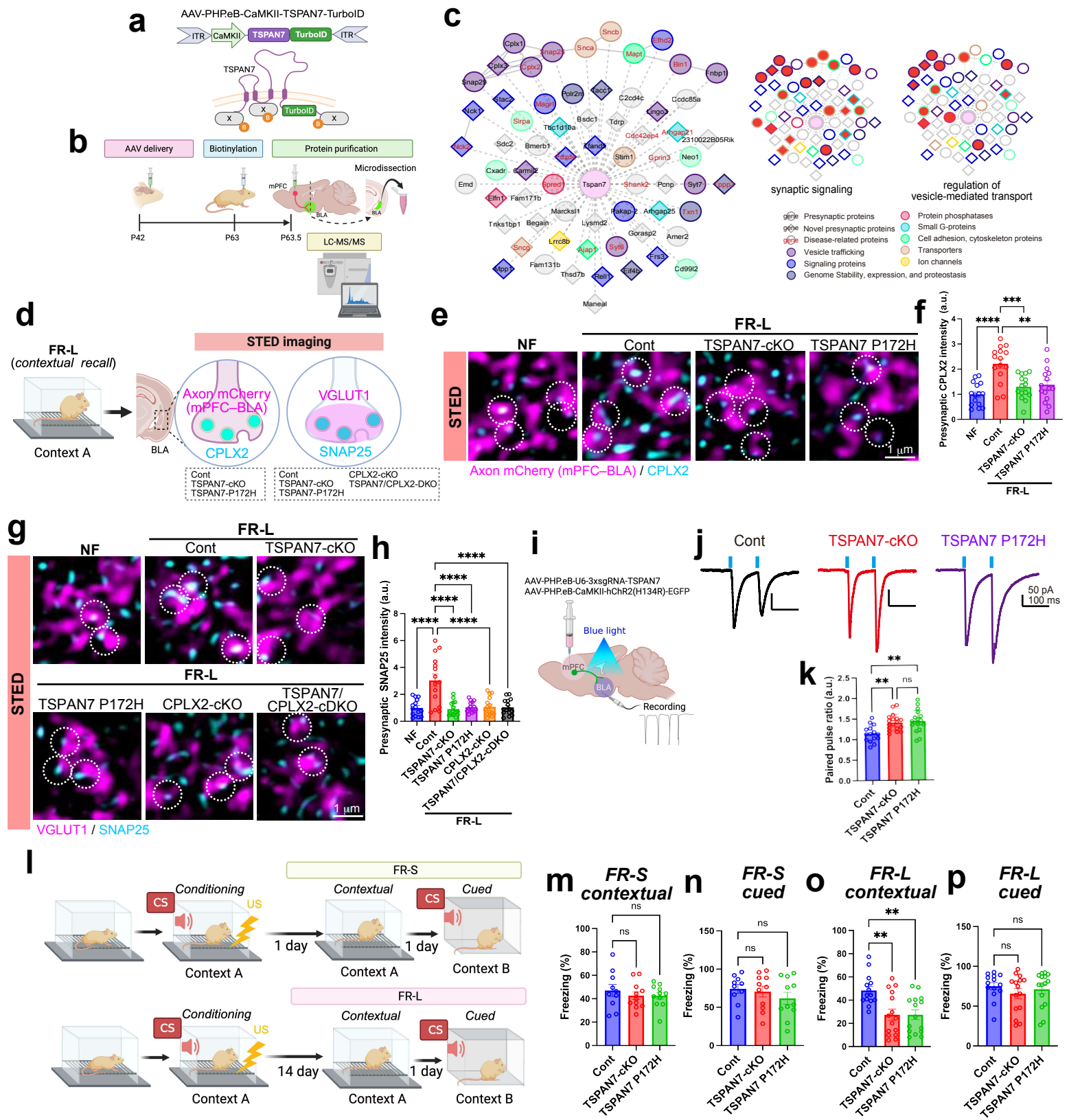


**Figure 4. TSPAN7–CPLX2 signalling promotes recall-associated presynaptic release-site remodelling and remote contextual fear memory in the mPFC–BLA pathway. a**, Schematic of the TSPAN7–TurboID fusion construct. **b**, Experimental design for *in vivo* TSPAN7–TurboID proteomic mapping of TSPAN7-proximal proteins in mPFC–BLA projection terminals. **c**, STRING-based protein network of TSPAN7–TurboID-enriched proteins. Node colouring follows the KEGG BRITE-based functional categories used in the protein–term network (Fig. 2a). Right panels highlight nodes annotated to the indicated GO terms. **d**, Experimental workflow for CPLX2 or SNAP25 immunostaining and STED imaging at mPFC–BLA presynaptic boutons under no-fear (NF) and remote contextual fear recall (FR-L) conditions. **e**, Representative STED images showing CPLX2 at mPFC–BLA presynaptic boutons in the BLA under NF and FR-L conditions. **f**, Quantification of CPLX2 signal intensity at mPFC–BLA presynaptic boutons in NF controls and FR-L mice of the indicated genotypes. Data are presented as mean ± s.e.m.; $n = 15$ slices from four mice per group. One-way ANOVA with Tukey's multiple-comparisons test. $^{****}P < 0.0001$, $^{***}P < 0.001$, $^{**}P < 0.01$; ns, not significant. **g**, Representative STED images showing VGLUT1 and SNAP25 at mPFC–BLA presynaptic boutons in the BLA under NF and FR-L conditions. **h**, Quantification of SNAP25 signal intensity at VGLUT1-positive presynaptic boutons in NF controls and FR-L mice of the indicated genotypes. Data are presented as mean ± s.e.m.; $n = 15$ slices from four mice per group. One-way ANOVA with Tukey's multiple-comparisons test. $^{****}P < 0.0001$. **i**, Schematic of optogenetic stimulation of mPFC–BLA projections and whole-cell recordings from BLA pyramidal neurons. **j**, Representative light-evoked excitatory postsynaptic currents (leEPSCs). **k**, Paired-pulse ratio (PPR) of leEPSCs across groups. Data are presented as mean ± s.e.m.; control $n = 15$ cells, TSPAN7-cKO $n = 18$ cells and TSPAN7 P172H $n = 18$ cells from 3–4 mice. One-way ANOVA with Tukey's multiple-comparisons test. $^{**}P < 0.01$; ns, not significant. **l**, Schematic of the fear-conditioning protocol and subsequent contextual or cued fear-recall tests performed at recent or remote time points. **m**–**p**, Freezing during recent contextual recall (**m**), recent cued recall (**n**), remote contextual recall (**o**) and remote cued recall (**p**). Data are presented as mean ± s.e.m.; control $n = 10$ (FR-S) or 14 (FR-L) mice, TSPAN7-cKO $n = 11$ (FR-S) or 15 (FR-L) mice and TSPAN7 P172H $n = 11$ (FR-S) or 15 (FR-L) mice from four independent experiments. One-way ANOVA with Dunnett's multiple-comparisons test. $^{**}P < 0.01$; ns, not significant.

## Supplementary Files

This is a list of supplementary files associated with this preprint. Click to download.

- SupplementalTable1.xlsx
- SupplementaryTable2.xlsx
- SupplementaryTable3.xlsx
- SupplementaryTable4.xlsx
- SupplementaryTable5.xlsx
- SupplementaryTable6.xlsx
- SupplementaryTable7.docx
- SupplementaryTable8.xlsx
- SupplementaryTable9.xlsx
- SupplementaryTable10.xlsx